

## THE EVOLUTION OF THE INNER REGIONS OF PROTOPLANETARY DISKS

EZEQUIEL MANZO-MARTÍNEZ,<sup>1</sup> NURIA CALVET,<sup>2</sup> JESÚS HERNÁNDEZ,<sup>3</sup> SUSANA LIZANO,<sup>1</sup> RAMIRO FRANCO HERNÁNDEZ,<sup>4</sup>  
CHRISTOPHER J. MILLER,<sup>2</sup> KARINA MAUCÓ,<sup>5,6</sup> CÉSAR BRICEÑO,<sup>7</sup> AND PAOLA D'ALESSIO<sup>1</sup>

<sup>1</sup>*Instituto de Radioastronomía y Astrofísica, Universidad Nacional Autónoma de México, Apartado Postal 3-72, C.P. 58089 Morelia, Michoacán, México*

<sup>2</sup>*Department of Astronomy, University of Michigan, 323 West Hall, 1085 South University Avenue, Ann Arbor, MI 48109, USA*

<sup>3</sup>*Instituto de Astronomía, Universidad Nacional Autónoma de México, Ensenada, México*

<sup>4</sup>*Instituto de Astronomía y Meteorología, Universidad de Guadalajara, México*

<sup>5</sup>*Núcleo Milenio Formación Planetaria - NPF, Universidad de Valparaíso, Av. Gran Bretaña 1111, Valparaíso, Chile*

<sup>6</sup>*Instituto de Física y Astronomía, Facultad de Ciencias, Universidad de Valparaíso, Av. Gran Bretaña 1111, 5030 Casilla, Valparaíso, Chile*

<sup>7</sup>*Cerro Tololo Inter-American Observatory, Casilla 603, La Serena 1700000, Chile*

(Received — —, — —; Revised — —, — —; Accepted — —, — —)

Submitted to ApJ

### ABSTRACT

We present a study of the evolution of the inner few au of protoplanetary disks around low-mass stars. We consider nearby stellar groups with ages spanning from 1 to 11 Myr, distributed into four age bins. Combining PANSTARSS photometry with spectral types we derive the reddening consistently for each star, which we use (1) to measure the excess emission above the photosphere with a new indicator of IR excess and (2) to estimate the mass accretion rate ( $\dot{M}$ ) from the equivalent width of the H $\alpha$  line. Using the observed decay of  $\dot{M}$  as a constrain to fix the initial conditions and the viscosity parameter of viscous evolutionary models, we use approximate Bayesian modeling to infer the dust properties that produce the observed decrease of the IR excess with age, in the range between 4.5  $\mu$ m and 24  $\mu$ m. We calculate an extensive grid of irradiated disk models with a two-layered wall to emulate a curved dust inner edge and obtain the vertical structure consistent with the surface density predicted by viscous evolution. We find that the median dust depletion in the disk upper layers is  $\epsilon \sim 3 \times 10^{-3}$  at 1.5 Myr, consistent with previous studies, and it decreases to  $\epsilon \sim 3 \times 10^{-4}$  by 7.5 Myr. We include photoevaporation in a simple model of the disk evolution and find that a photoevaporative wind mass-loss rate of  $\sim 1 - 3 \times 10^{-9} M_{\odot} yr^{-1}$  agrees with the decrease of the disk fraction with age reasonably well. The models show the inward evolution of the H<sub>2</sub>O and CO snowlines.

*Keywords:* accretion, accretion disks — circumstellar matter — stars: pre-main sequence — stars: variables: T Tauri, Herbig Ae/Be

### 1. INTRODUCTION

Protoplanetary disks are natural byproducts of the star formation process, and the sites where new planetary systems will emerge (Williams & Cieza 2011; Testi et al. 2014). Stars surrounded by protoplanetary disks exhibit excess flux over the photosphere from the infrared to millimeter wavelengths due to emission by dust particles; thus the spectral energy distribution (SED) of the system is directly related to the structure and the physical conditions of the dusty component of the disk (D'Alessio et al. 1998, 2001, 2006). In addition, disks are accreting mass onto the star and releasing accretion energy; this accretion energy appears as a continuum excess that veils the photospheric lines and

dominates in the UV continuum and in emission lines (Calvet & Gullbring 1998; Hartmann et al. 2016).

Protoplanetary disks show direct evidence of evolution. Studies of disks in populations ranging from  $\sim 1$  to 10 Myr indicate that the number of disk-bearing stars decreases with age, from a frequency of  $\sim 70\%$  at 1 Myr to  $< 10\%$  by 10 Myr (Hernández et al. 2007a, 2008; Briceño et al. 2019). The frequency of stars accreting mass from their disk also decreases with age, in proportions similar, but not equal, to the frequency of inner disks estimated from dust emission (Fedele et al. 2010; Briceño et al. 2019).

It has also been found that the mass accretion rate decreases with age (Hartmann et al. 1998, 2016, and references therein), which is consistent with the viscous evo-

lution of self-similar disks (Lynden-Bell & Pringle 1974; Hartmann et al. 1998).

In addition, it has also been found that the median strength of the near-infrared excess in disks of a given population decreases as the age of the population increases (Hernández et al. 2007b; Luhman et al. 2010). The IR excess arises from emission from dust in the disk, which initially constitutes about 1% of the total mass. The observed decrease of the strength of the excess may be consistent with the decrease of total disk mass with time resulting from viscous evolution. Alternatively, in addition to gas evolution, the decay of emission may require dust evolution, such as growth and settling towards the midplane (Weidenschilling 1997; Dullemond & Dominik 2004; Birnstiel et al. 2009, 2010, 2011). Despite recent progress, details of the processes leading to the decrease of dust emission with age are still uncertain.

Disk censuses using broad band photometric SEDs indicate that the decrease of IR emission leading to the evolution from optically thick full primordial disks to optically thin debris disks follows at least two evolutionary path-ways (Hernández et al. 2007b; Merín et al. 2010; Cieza et al. 2007; Williams & Cieza 2011). One is represented by the *evolved disks* in which the flux at all bands decreases with age (Hernández et al. 2008; Luhman et al. 2010), suggesting a gradual depletion of dust at all disk radii (Merín et al. 2010). These disks are known as evolved (used here), “anemic”, “homologously depleted”, and “homogeneously draining” (Lada et al. 2006; Currie et al. 2009; Koepferl et al. 2013) and no large inner cavities are detectable in their SEDs.

Another path-way of disk evolution comes from observations of inner disk zones cleared of small dust, which appear as flux deficits in the near-IR in the *transitional disks* (TDs). Observationally, classical TDs have been defined as protoplanetary disks with little or no near-IR excess ( $\lambda \lesssim 10\mu\text{m}$ ) and significant excess comparable to the median of Taurus (Maucó et al. 2016; Furlan et al. 2006) at longer wavelengths (Strom et al. 1989; Calvet et al. 2002, 2005). Several explanations have been given for opening holes in the inner disk: dynamical clearing by planets, photoevaporation and viscous evolution, dust grain growth, differential dust drift, dead zones and condensations fronts (Zhu et al. 2011, 2012; Espaillat et al. 2014; Owen 2016; Alexander et al. 2014; Chiang & Murray-Clay 2007; Dullemond & Dominik 2005; Birnstiel et al. 2012; Pinilla et al. 2016; Zhang et al. 2015). The *pre-transitional disks* (PTDs Espaillat et al. 2007, 2010), those with an optically thick inner ring inside their large cavities, may correspond to a phase of evolution previous to TDs in which the innermost disk has not yet completely dissipated. The most accepted explanation is that the large gaps are due to planets, which have already been found in the cleared regions of pre-

transitional disks (Keppler et al. 2019; Haffert et al. 2019).

ALMA high angular resolution observations at sub-millimetric wavelengths have shown that structure is ubiquitous in protoplanetary disks, with multiple rings and spiral arms detected in numerous disks (ALMA Partnership et al. 2015; Andrews et al. 2016, 2018); TDs and PTDs are extremes cases in which the dust structure also appears in the SED. Several interpretations have been suggested for these structures. For instance, large dust particles get trapped at the edges of gaps opened by forming planets, resulting in bright rings (Zhang et al. 2018). Alternatively, the gaps could be due to changes in the dust properties, as happens in sublimation fronts (Zhang et al. 2015). In any event, observations of disk structures are biased towards the bright and largest disks, those that can be resolved (Andrews et al. 2018; Long et al. 2018, 2019). On the other hand, except for the TDs, disks with detected structure share the same location in near and mid-IR color-color diagrams than unresolved disks (cf. IRAC colors in Hartmann et al. 2005), which suggests a common overall evolution, at least at the inner regions.

Several studies give different estimates for the relative numbers of (pre)transitional and evolved disks in populations of different ages. Part of these differences arises because the criteria to define a transitional or an evolved disk are far from homogeneous (Williams & Cieza 2011). In this contribution we use the observational definition of TD as given above, which physically corresponds to disks with inner holes of tens of au (Espaillat et al. 2012, 2014). This kind of disks represent <10-20% of the total disk population in young stellar clusters (Muzerolle et al. 2010). Our focus in this work will be the rest of the disks, which encompass the “weak” and “warm” excess disks of Muzerolle et al. (2010), the “primordial ultra-settled” and the “homogeneous draining” of Koepferl et al. (2013) and Ercolano et al. (2015), the “anemic” of Currie et al. (2009), and the “evolved” of Hernández et al. (2008) and Luhman et al. (2010).

We carry out a new disks census including well known nearby young stellar groups studied using IRAC photometry (3.6, 4.5, 5.8 and 8  $\mu\text{m}$ ; Fazio et al. 2004) and the 24  $\mu\text{m}$  MIPS photometry (Rieke et al. 2004). In general, we also use optical PANSTARRS data (Chambers et al. 2016) to trace the stellar photosphere of the disk-bearing stars. These groups have ages between 1 and 11 Myr, the critical age range where significant disk evolution takes place (Hernández et al. 2007a). We study the evolution of dust using a new indicator of the flux excess over the photosphere in the near and mid-IR, between 4.5  $\mu\text{m}$  and 24  $\mu\text{m}$ . We also use the D’Alessio irradiated accretion disk (DIAD) models to infer the state of the dust at a given age using approximate Bayesian modeling, and in particular, we focus on indicators of dust settling at two size scales, at  $\sim 0.1$  au and at  $\sim 10$  au, to explore the degree of inner disk

clearing. In addition, in contrast to previous works, we include the decrease of the observed mass accretion rate with age as an additional constraint in the evolution.

The structure of this paper is the following. In Section 2, we present the general properties of the stellar populations studied in this work, calculate disks excesses and mass accretion rates, and discuss how they change with age. In Section 3 we describe the disk models that we use to interpret the observations, and the results inferred from using these models to interpret the disk evolution indicators. In Section 4 we discuss our results and put them in context of what we know from previous studies. Finally, in Section 5 we summarize and present our conclusions.

## 2. OBSERVED DISK EVOLUTION

### 2.1. Sample of stellar populations

To make a comprehensive statistical study of the evolution of disks around T Tauri stars (TTSs), we selected nearby ( $\lesssim 500$  pc), young ( $\sim 1$  to 11 Myr old) stellar groups with Spitzer photometry and with available spectroscopic information for most of the TTSs reported in each stellar group. The populations included in this work are (see Table 1): the Orion Nebula Cluster (ONC), Taurus, the IC348 cluster, the  $\sigma$  Orionis cluster ( $\sigma$  Ori), the  $\lambda$  Orionis cluster ( $\lambda$  Ori), the Orion OB1b subassociation (Ori OB1b), the Upper Scorpius subassociation (UpSco), the  $\gamma$  Velorum cluster ( $\gamma$  Vel), and the Orion OB1a subassociation (Ori OB1a), which includes the stellar aggregates 25 Ori, HD 35762, and HR 1833.

For each group, we compiled stars with spectral types ranging from K0-M6. To study the evolution of the dust component of the disk (§2.3 & 2.5), we only selected stars with additional IRAC photometry in all four bands. In §2.3 we describe the methodology followed to separate the disk-bearing stars from the rest, in each stellar group. To study the gas component of the disk (§2.6), we use a different sample from the one used to study the dust component, since in this case we selected confirmed TTSs with existing equivalent width of  $H\alpha$  (EW  $H\alpha$ ), measured using the SpTClass tool (Hernández et al. 2004; Hernandez et al. 2017), and with GAIA DR2 parallaxes with relative errors  $\lesssim 20\%$ , regardless of whether or not they have IRAC photometry. This means that some stars in the sample used to calculate mass accretion rates additionally have IRAC photometry and thus they also belong to the sample used to study the dust component. However there are stars which do not have IRAC photometry, while having the necessary information to determine the corresponding mass accretion rate. As a consequence, there are stars in this sample of accretors, which do not belong to the sample used to study the dust component using color excesses and accordingly, there are stars with color excesses for which  $\dot{M}$  could not be determined.

In general, we use the color  $[g - i]$  from PANSTARRS (Chambers et al. 2016) to estimate homogeneously visual extinctions for the samples of TTSs (see §2.2). Thus we also require that the TTSs have  $g$  and  $i$  magnitudes reported by PANSTARRS <sup>1</sup>. Table 1 shows the stellar populations included in this work with their general properties taken from the literature, except for the last four columns. Based on both the stellar ages and disk frequencies previously reported, we grouped the stellar population into four age bins (see last column of Table 1).

#### 2.1.1. ONC

The ONC is a very young stellar cluster ( $\sim 1 - 3$  Myr; Hillenbrand 1997; Hillenbrand et al. 2013; Da Rio et al. 2010; Megeath et al. 2016) with a mean distance of  $\sim 400$  pc (Briceño et al. 2019, using GAIA DR2 data). Also Briceño et al. (2019) estimate a disk frequency of  $\sim 73 \pm 5.9\%$ . The initial sample of TTSs includes 782 stars with spectral types, equivalent widths of Li I  $\lambda 6708\text{\AA}$  (EW LiI), and EW  $H\alpha$  obtained from the analysis of low-resolution spectra observed with the fiber-fed multi-object Hectospec instrument mounted on the 6.5 m Telescope of the MMT Observatory (Hernández et al. 2020a, in preparation). We also include 127 TTSs with spectral types, EW LiI, and EW  $H\alpha$  reported by Briceño et al. (2019). Spectral types, EW LiI, and EW  $H\alpha$  in Hernández et al. 2020a (in preparation) and Briceño et al. (2019) were obtained using the SpTClass code (Hernandez et al. 2017), an IRAF/IDL code based on the methods described in Hernández et al. (2004). We complete the initial sample adding 86 TTSs and 48 TTSs with spectral types reported by Hillenbrand (1997) and Hillenbrand et al. (2013), respectively. Out of 1036 TTSs in the initial sample, 500 TTSs have IRAC/MIPS photometry reported by Megeath et al. (2012). We also include 170 additional TTSs with IRAC/MIPS photometry provided by Tom Megeath (private communication) which were not included in Megeath et al. (2012). Finally, out of 670 TTSs with IRAC/MIPS photometry, we select 508 TTSs with  $g$  and  $i$  magnitudes from PANSTARRS.

#### 2.1.2. Taurus

Taurus is one of the best studied and closest star-forming molecular cloud complexes, with an estimated age of  $\sim 1 - 2$  Myr (Luhman et al. 2010; Furlan et al. 2011). Using data from Luhman et al. (2010) we estimate a disk frequency of this complex of  $\sim 63.7 \pm 5.1\%$  for K0-M6 stars. Based on distances provided by GAIA DR2 and Very Long Baseline Interferometry (VLBI) ob-

<sup>1</sup> Except for the  $\gamma$  Velorum cluster, which was not observed by the PANSTARRS survey

**Table 1.** Stellar Groups

Group	Mean distance	Age	Disk fraction	References	Initial	Disk-bearing	Accretors	Age
	pc	Myr	%		sample	stars	sample	bin
ONC	400	1-3	73±5.9	4,7,4	508	305	228	1
Taurus	130-200	1-2	63.7±5.1	8,9,*	137	87	16	1
IC348	320	2-3	47±12	10,1,1	163	59	...	2
$\sigma$ Ori	400	3	36±4	11,2,2	185	73	40	2
$\lambda$ Ori	400	4-6	18.5±4	12,3,3	142	24	...	3
Ori OB1b	400	5	13-17	4,6,4	278	45	59	3
Upper Sco.	146	5-11	25±0.02	13,14,9	59	19	...	3
$\gamma$ Vel	345	7.5	5-7	15,16,5	125	14	...	4
Ori OB1a	350-360	9-14	6-10	4,4,6	189	13	77	4

NOTE—References: (1) Lada et al. (2006), (2) Hernández et al. (2007a), (3) Hernández et al. (2010), (4) Briceño et al. (2019), (5) Hernández et al. (2008), (6) Hernández et al. (2007b), (7) Hillenbrand et al. (2013), (8) Galli et al. (2019), (9) Luhman & Mamajek (2012), (10) Ortiz-León et al. (2018), (11) Pérez-Blanco et al. (2018), (12) Kounkel et al. (2018), (13) Galli et al. (2018), (14) David et al. (2019), (15) Franciosini et al. (2018), (16) Jeffries et al. (2017). \*Using the data from Luhman et al. (2010) we estimate a disk fraction of  $63.7 \pm 5.1$  in Taurus.

NOTE—Column 6 refers to the number of K0-M6 stars initially compiled (diskless and disk-bearing stars) with IRAC and PANSTARRS photometry in each stellar group. Column 7 refers to the number of stars with near-IR excess above the photosphere, separated according to §2.3, which correspond to the sample used to study the dust component of the disks. Column 8 refers to the CTTSs/CWTTTSs sample, described in §2.6.1 used to study the evolution of  $\dot{M}$ .

servations, Galli et al. (2019) show that the Taurus star forming complex includes several molecular clouds located at different distances (from  $\sim 130$  pc to  $\sim 200$  pc). Based mostly on the work of Hartmann et al. (2005) and Luhman et al. (2010), Esplin et al. (2014) compiled 414 members of Taurus with IRAC/MIPS photometry. From this sample, we selected 260 TTSs with measurements in all the photometric bands of IRAC and with spectral types ranging from K0 to M6. In some cases, stars identified as binary stars have spectral types for the two components (e.g. M1+M7); in this case we select the spectral type of the brighter component (e.g. M1). Out of 260 TTSs, 137 TTSs have  $g$  and  $i$  photometry from PANSTARRS. A sample of 100 TTSs have optical low resolution spectra available from the FAST Public Archive<sup>2</sup>. We have measured EW H $\alpha$  in this work for this sample using the SpTClass tool (Hernandez et al. 2017).

### 2.1.3. IC348

IC348 is a nearby and compact young cluster ( $\sim 2$ -3 Myr) located in the Perseus OB2 star forming region (Lada et al. 2006; Herbst 2008). Combining trigonometric parallaxes from Very Long Baseline Array (VLBA) observations and GAIA DR2 parallaxes, Ortiz-León et al. (2018) estimate a distance of  $\sim 320$  pc for this cluster. Lada et al. (2006) estimated a disk frequency of  $\sim 47 \pm 12\%$  and provide spectral types and IRAC/MIPS photometry for 307 stars in the IC348

cluster. From this set, we selected 220 stars with spectral types ranging from K0 to M6 and with photometric measurements in all IRAC bands. Out of 220 TTSs, 163 TTSs have PANSTARRS  $g$  and  $i$  magnitudes.

### 2.1.4. $\sigma$ Ori

$\sigma$  Ori is a young ( $\sim 3$  Myr) and relatively populous stellar cluster located in the Orion OB1b sub association and with a disk frequency of  $\sim 36 \pm 4\%$  (Hernández et al. 2007a). Using GAIA DR2 parallaxes, Pérez-Blanco et al. (2018) estimate a mean distance of  $\sim 400$  pc. We have selected 221 TTSs with spectral types ranging from K0 to M6, EW LiI, and EW H $\alpha$  obtained by Hernández et al. (2014) using the SpTClass tool and with photometric measurements in all IRAC bands (Hernández et al. 2007a). From this sample, 185 TTSs have PANSTARRS  $g$  and  $i$  magnitudes.

### 2.1.5. $\lambda$ Ori

$\lambda$  Ori is a young ( $\sim 4$ -6 Myr) and relatively populous stellar group with an overall disk frequency for M type stars of  $\sim 18.5 \pm 4\%$  (Hernández et al. 2010). Combining spectroscopic and astrometric data from APOGEE-2 and GAIA DR2, Kounkel et al. (2018) reported an average distance of  $\sim 400$  pc for this stellar cluster. Spectral types were compiled from Bayo et al. (2011) and Sacco et al. (2008). We also add stars with effective temperatures reported by Bayo et al. (2008) and Bayo et al. (2011). Those effective temperatures were converted to spectral types using Table 6 from

<sup>2</sup> <http://tdc-www.harvard.edu/cgi-bin/arc/fsearch>



Pecaut & Mamajek (2013). From this compilation we have selected 181 TTSs with spectral types ranging from K0 to M6 and with photometric measurements in all IRAC bands (Hernández et al. 2010). From this sample, we select 142 TTSs with PANSTARRS  $g$  and  $i$  magnitudes.

#### 2.1.6. Ori OB1b

Briceño et al. (2019) report EW LiI and EW H $\alpha$  for 551 TTSs with spectral types ranging from K0 to M6 located in this subassociation. Based on GAIA DR2 parallaxes and the PMS models of Siess et al. (2000), Briceño et al. (2019) adopted a distance of 400 pc and a stellar age of  $\sim 5$  Myr. The disk frequency in Ori OB1b is  $\sim 13 - 17\%$  (Hernández et al. 2007b; Briceño et al. 2019). Out of 551 TTSs, 104 and 213 TTSs have photometric measurements in all IRAC bands provided by Hernández et al. (2007b) and Hernández et al. 2020b (in preparation), respectively. From this sample, we select 278 TTSs with PANSTARRS  $g$  and  $i$  magnitudes.

#### 2.1.7. Upper Sco

Upper Sco is the youngest stellar population of the Scorpius-Centaurus OB association, which is the nearest region of recent massive star formation (Preibisch & Mamajek 2008). Based on the GAIA first data release, Galli et al. (2018) estimate a mean distance of  $\sim 146$  pc. Stellar ages estimated for Upper Scorpius range from  $\sim 5$  (Preibisch et al. 2002) to 11 Myr (Pecaut et al. 2012) and recently, using eclipsing binaries, David et al. (2019) estimate an age of 5-7 Myr. Out of 306 stars in Luhman & Mamajek (2012) with spectral types ranging from K0 to M6, 74 stars have protoplanetary disks. The disk frequency reported by Luhman & Mamajek (2012) is  $\sim 25 \pm 0.02\%$  for Upper Scorpius. Out of 306 K and M stars, 90 stars have photometric measurements in all IRAC bands. Finally, out of 90 stars, we select 59 stars with PANSTARRS  $g$  and  $i$  magnitudes.

#### 2.1.8. $\gamma$ Vel

$\gamma$  Vel is a young stellar cluster with a central binary system consisting of an O7.5 star and a Wolf-Rayet star (WC8; Hernández et al. 2008). Based on GAIA DR2 observations, Franciosini et al. (2018) estimate a distance of  $\sim 345$  pc. The stellar age of the  $\gamma$  Velorum cluster can range from 5 Myr to 20 Myr, with an age of  $7.5 \pm 1$  Myr inferred from the color-magnitude diagram (Jeffries et al. 2017). The disk frequency of the cluster is  $\sim 5 - 7\%$  (Hernández et al. 2008). Out of 557 stars with optical photometry (V, I $_c$ ) and IRAC photometry in all bands (Hernández et al. 2008), we compile 125 stars with effective temperatures lower than 5000 K (e.g. spectral type K0 or

later; Pecaut & Mamajek 2013) reported by Spina et al. (2014), Frasca et al. (2015) or Smiljanic et al. (2016). From the sample of 125 stars, 11 do not have reported spectral types or effective temperature, thus we estimate their stellar mass using the  $[V - I_c]$  vs stellar mass relation from Prisinzano et al. (2016), then we estimate their effective temperature from the relation  $T_{\text{eff}} = 1005.78 M_* + 3042.1$  (Frasca et al. 2015). Since  $\gamma$  Vel is out of the area coverage of the PANSTARRS survey, we estimate visual extinction using the  $[V - I_c]$  color instead the  $[g - i]$  color (see §2.2).

#### 2.1.9. Ori OB1a

Briceño et al. (2019) report EW LiI and EW H $\alpha$  for 1211 TTSs with spectral types ranging from K0 to M6 located in this sub-association. This sample includes 807 TTSs located in the dispersed population of Ori OB1a, and 404 TTSs members of the stellar groups 25 Ori, HR 1833, and HD 35762. Since some TTSs of the dispersed population of Ori OB1a are located close to other younger stellar groups, we rejected 100 TTSs located near the  $\lambda$  Ori star forming region ( $\text{DEC} > 4^\circ$ ) or near the Ori OB1b subassociation ( $\text{DEC} < -2^\circ$ ). Based on GAIA DR2 parallaxes and the PMS models of Siess et al. (2000), Briceño et al. (2019) adopted a distance of 350-360 pc with a stellar age range of  $\sim 9-14$  Myr. The disk frequency for the Orion OB1a subassociation is  $\sim 6 - 10\%$  (Hernández et al. 2007b; Briceño et al. 2019). Out of 1211 TTSs, 121 and 93 TTSs have photometric measurements in all IRAC bands, reported in Hernández et al. (2007b) and Hernández et al. 2020b (in preparation), respectively. From this sample, we select 189 TTSs with PANSTARRS  $g$  and  $i$  magnitudes.

### 2.2. Visual extinctions, stellar luminosities and stellar masses

In general, we calculate the extinction  $A_V$  for each star in our samples, using the  $[g - i]$  color from PANSTARRS. One of the advantages of using PANSTARRS photometry is that this survey was performed several times per filter, over a four-year time span, which addresses the effects of variability when using the reported mean magnitude. The intrinsic photospheric color  $[g - i]_0$  was added to Table 6 from Pecaut & Mamajek (2013) using the following relation between the color  $[V - I_c]$  and the PANSTARRS color  $[g - i]$ :

$$[g - i] = 0.475(\pm 0.019) + 0.751(\pm 0.007) [V - I_c]. \quad (1)$$

This relation was obtained using a sample of confirmed TTSs with both  $[V - I_c]$  color reported by Briceño et al. (2019) and  $[g - i]$  color from PANSTARRS.

We use Table 6 from Pecaut & Mamajek (2013) to interpolate the spectral types, and obtain the effective temperature  $T_{\text{eff}}$ , the bolometric correction for the  $J$  band ( $BC_J$ ), and the intrinsic color  $[g - i]_o$ . The extinction  $A_V$  is estimated from the  $[g - i]$  color using the standard interstellar reddening law ( $R_V=3.1$ ) and relations from Cardelli et al. (1989), with a central wavelength of  $0.481 \mu\text{m}$  and  $0.752 \mu\text{m}$  for the  $g$  and  $i$  band, respectively (Tonry et al. 2012).

Since PANSTARRS does not cover the region of  $\gamma$  Vel, the extinction  $A_V$  for this stellar cluster is estimated from the color  $[V - I_c]$  and the standard interstellar reddening law, and the relation from Cardelli et al. (1989), with a central wavelength of  $0.79 \mu\text{m}$  for the  $I_c$  filter. The intrinsic color  $[V - I_c]_o$  was estimated interpolating the effective temperature in Table 6 from Pecaut & Mamajek (2013).

We estimate stellar luminosities for TTSSs with uncertainties in parallaxes below 20% (Gaia Collaboration et al. 2018). Thus, distances can be calculated as the inverse of the parallaxes (Bailer-Jones 2015). We derive the absolute bolometric magnitude from the absolute  $J$  magnitude and the bolometric correction  $BC_J$  from Pecaut & Mamajek (2013). The 2MASS  $J$  magnitudes (Cutri et al. 2003) were corrected for extinction using the derived  $A_V$  and the standard reddening law. Finally, the luminosities are obtained using  $M_{\text{bol}} = 4.74$  for the Sun.

The stellar mass ( $M_*$ ) is obtained by performing a double interpolation in the H-R diagram using the Pre-Main Sequence (PMS) models of Siess et al. (2000). Some stars have luminosity or effective temperature out of the range of these stellar evolutionary models, hence their mass cannot be determined.

### 2.3. Disk color excess

We introduce the disk color excess (hereafter DCE) as a new indicator of disk infrared excesses to gauge the global dust evolution. This indicator takes into account not only the extinction correction of infrared colors used as disk tracers, but also the photospheric contribution for a given spectral type. We use the  $J$  band as anchor of the colors to measure the infrared excesses over the photosphere because this band is representative of the stellar photosphere of TTSSs, since it is less contaminated by infrared excesses produced by the dust component in the disk or by excess emission from accretion shocks than other optical-red bands. For each star in each population described in §2.1, we define the DCE for each Spitzer color  $[J - \lambda_{IR}]$  as:

$$DCE_{J-\lambda_{IR}} = [J - \lambda_{IR}]_{\text{obs}} - [J - \lambda_{IR}]_o - \left( \frac{A_J}{A_V} - \frac{A_{\lambda_{IR}}}{A_V} \right) \times A_V, \quad (2)$$

where  $\lambda_{IR}$  represents the Spitzer magnitudes [3.6], [4.5], [5.8], [8.0] and [24], and  $[J - \lambda_{IR}]_o$  represents the in-

trinsic Spitzer photospheric colors. The selective extinctions,  $A_{3.6}/A_V=0.048$ ,  $A_{4.5}/A_V=0.035$ ,  $A_{5.8}/A_V=0.024$ ,  $A_{8.0}/A_V=0.031$ , and  $A_{24}/A_V=0.015$ , are estimated interpolating the central wavelengths of each filter using Table 21.6 from Allen’s Astrophysical Quantities (Reipurth 2008) assuming a standard interstellar law. We estimate the photospheric Spitzer colors,  $[J - 3.6]_o$ ,  $[J - 4.5]_o$ ,  $[J - 5.8]_o$ ,  $[J - 8.0]_o$  and  $[J - 24]_o$ , by interpolating the spectral types in Table 13 from Luhman et al. (2010). For K-type stars earlier than K4, we assume the photospheric Spitzer colors of a K4 star. This approximation is in agreement within 1% with empirical photospheric colors in the spectral type range K0-K4 (K. Luhman internal communication). At each age bin, the observational sample contains at most 3 K0-K4 stars (cf. Figure 3), thus the estimated Spitzer colors are not affected, since the total sample used in each age bin is much larger than the number of K0-K4 stars.

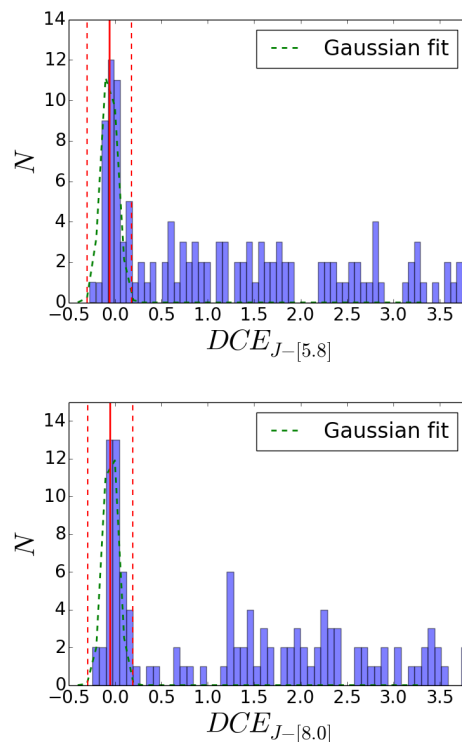


**Figure 1.**  $DCE_{J-[5.8]}$  distribution (upper panel) and  $DCE_{J-[8.0]}$  distribution (lower panel) for stars in the Taurus sample. The green line is the Gaussian fit to the distribution of DCEs and the red lines are the mean (solid line) and the  $3\sigma$  limits (dashed lines).

For each stellar group, we separate the disk-bearing stars from the diskless stars using the distributions of  $DCE_{J-[5.8]}$  and  $DCE_{J-[8.0]}$ . As an illustration, Figure 1 shows these distributions for Taurus. We estimate the photospheric region by fitting a Gaussian function (green dashed line) to the DCE distributions around the

photospheric values (e.g.  $DCE \sim 0$ ). We apply the  $3\sigma$ -clipping method, which consists of calculating the center value ( $C_G$ ) and the standard deviation ( $\sigma_G$ ) of the Gaussian function and redo the Gaussian fitting for stars within the range  $C_G - 3 \times \sigma_G < DCE < C_G + 3 \times \sigma_G$ . This process is repeated until the values for the center and  $\sigma$  of the Gaussian function converge. In our populations, these values converge in less than 4 iterations. The final value of  $C_G + 3 \times \sigma_G$  is used to set the limit that separates disk-bearing stars from those with photospheric values. To avoid stars with evolutionary stages earlier than Class II objects (e.g. protostars), the upper limits for disk-bearing stars are set by estimating the DCEs associated to a flat SED ( $DCE_{J-[5.8]}=4.28$ ;  $DCE_{J-[8.0]}=5.30$ ). Thus, the disk-bearing stars sample is defined as those stars between the photospheric limit and the flat SED limit. The number of TTSs selected as disk-bearing stars in each stellar population is indicated in Table 1 (column 7).

Figure 2 shows the  $DCE_{J-[5.8]}$  color versus the  $DCE_{J-[8.0]}$  color for the stellar groups described in section 2.1, highlighting the disk-bearing sample (red) selected to study the global evolution of the dusty component of the disk. The green points in the upper right corner in the Taurus panel correspond to stars in evolutionary stages earlier than Class II objects. Following equation (2) we calculate, besides the DCEs  $J-[5.8]$  and  $DCE_{J-[8.0]}$ , the rest of the DCEs ( $J-[3.6]$ ,  $J-[4.5]$  and  $J-[24]$ ) for the disk-bearing sample. Since the MIPS photometry is less deep than the IRAC observations and the MIPS coverage can be slightly different from the IRAC coverage, some disk-bearing stars do not have an estimation of  $DCE_{J-[24]}$ . This bias can affect mainly the disk-bearing stars with the smallest values of  $DCE_{J-[5.8]}$  and  $DCE_{J-[8.0]}$ . As an illustration, Figure 3 shows the distribution of spectral types for all the disks-bearing stars (purple) and for the stars with MIPS 24 detections (pink) in all age bins (see §2.4). The main difference in these distributions can be observed for stars with the latest spectral types.

#### 2.4. Separation into age bins

Since our goal is to make a study with good statistical significance, we grouped the disk-bearing sample selected in each stellar population into 4 groups or age bins. We take into account two criteria to group the disk-bearing sample into the four age bins: their nominal age, obtained by fitting one isochrone to the location of all the stars of a given stellar group in the H-R diagram, and their disk fraction (see Table 1). Following these criteria, we separate the populations into the following age bins:

- Bin 1 (1-2 Myr): ONC and Taurus
- Bin 2 (2-3 Myr): IC348 and  $\sigma$ -Ori

**Table 2.** Observed stellar masses

bin	mean ( $M_*/M_\odot$ )	$\sigma$
1	0.33	0.24
2	0.30	0.20
3	0.29	0.22
4	0.28	0.22

- Bin 3 (3-5 Myr):  $\lambda$  Ori, Ori OB1b, and Upper Sco
- Bin 4 (5-11 Myr):  $\gamma$  Vel and Ori OB1a

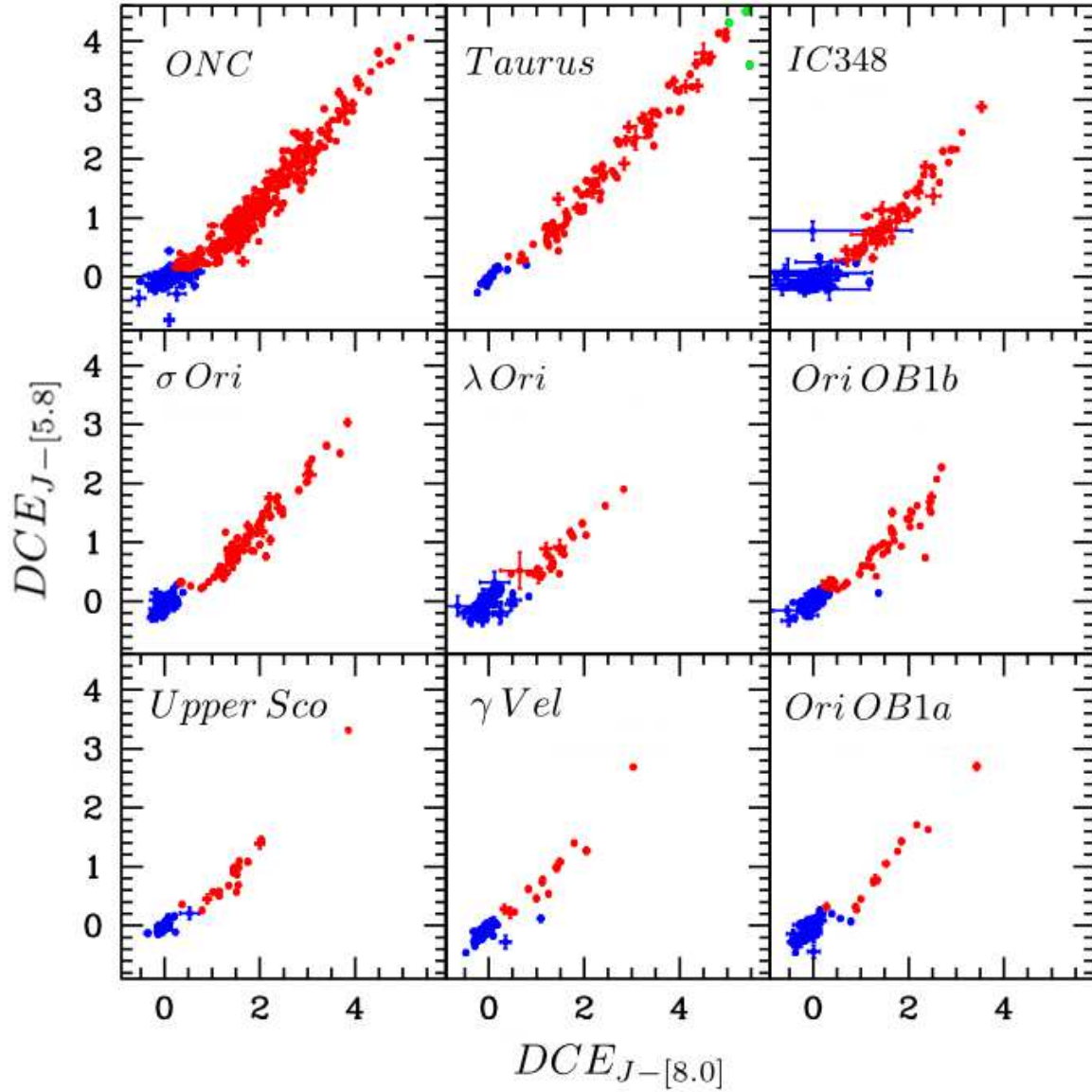
Table 1 shows properties of all stellar populations in §2.1 and the age bin we assigned to them. We assigned Upper Scorpius to the third age bin, in agreement with its disk fraction and with the age (5-7 Myr) recently determined by David et al. (2019), although some authors suggest it is older ( $\sim 11$  Myr, Pecaut et al. 2012; Song et al. 2012). To test the goodness of our assemblage of age bins, we plot the median of the stellar luminosity estimated in §2.2 vs the age of each bin (Figure 4). It is apparent that the median of the stellar luminosity decreases with age, consistent with expectations from stellar evolution, since most stars in each bin are late K and M as shown in Figure 3, and thus are evolving along Hayashi tracks.

Figure 5 shows the distribution of stellar masses per age, including stars with determinations of mass accretion rates (§2.6.1). The mean value of the observed stellar masses in all age bins is  $\sim 0.3 M_\odot$  (see Table 2).

#### 2.5. The evolution of the disk color excess

For each age bin we build histograms for the observed DCEs in the IRAC and MIPS 24 bands, which are shown in Figure 6, where we notice that the “tails” located at the right of the distributions (e.g.  $DCE_{J-[4.5]} \gtrsim 2$ ) in the youngest bin, disappear as the age increases, while the position of the peak of the distributions remains approximately in the same position, with the exception of the color  $DCE_{J-[24]}$ , in which the peak moves towards smaller values with age. Figure 7 shows the median of the DCE distributions as a function of age; the quartiles, shown as error bars, indicate the range where 50% of the disk-bearing stars are located. We performed a two-sample KS-test on the different DCE distributions for all the age bins and found the  $p$ -values shown in Table 3. In general, these values indicate different DCE distributions between bin 1 and bin 2 ( $p$ -value  $< 6\%$ ) which suggest significant dust evolution between these two bins. In contrast, the KS-test indicates no difference between the DCE distributions in bin 3 and bin 4 ( $p$ -value  $> 90\%$ ) suggesting little or no dust evolution between these older bins.

Although the distance to each star is not used to calculate the observed DCEs, an additional constrain to add



**Figure 2.**  $DCE_{J-[5.8]}$  vs  $DCE_{J-[8.0]}$  diagrams for all stellar groups. Red dots correspond to the stars with excess at  $5.8\ \mu\text{m}$  and  $8\ \mu\text{m}$  and blue dots are stars without excess. The green points in the Taurus panel are objects in early stages than Class II objects.



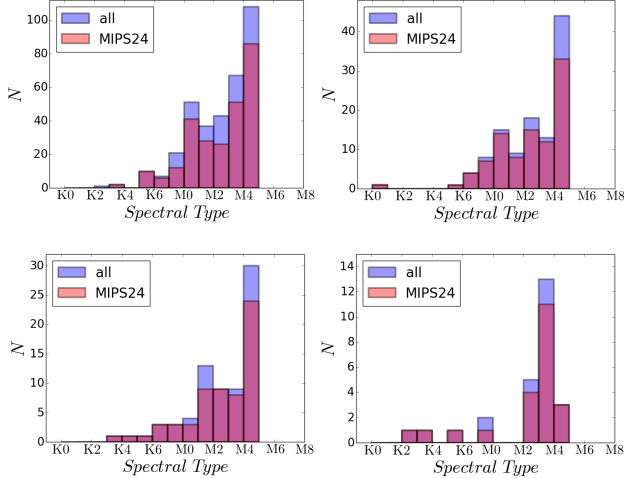


**Figure 3.** Distribution of spectral types at 1.5 Myr (bin 1, upper left), 2.5 Myr (bin 2, upper right), 4.5 Myr (bin 3, lower left) and 7.5 Myr (bin 4, lower right). Bin 1, 2, 3 and 4 comprehend 1-2, 2-3, 3-5 and 5-11 Myr, respectively. The purple distribution comes from all the stars in our sample, while the pink one corresponds to stars with MIPS 24 detections.

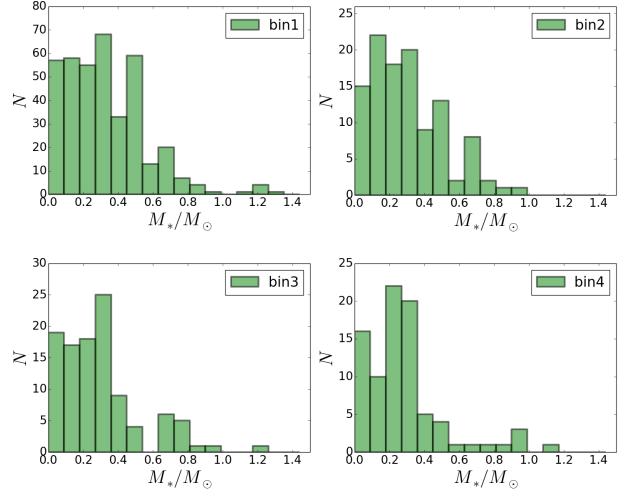


**Figure 5.** Distribution of stellar masses in all bins.

**Table 3.** KS-test  $p$ -values

bins	$DCE_{J-[4.5]}$	$DCE_{J-[5.8]}$	$DCE_{J-[8.0]}$	$DCE_{J-[24]}$
1-2	0.04	0.05	0.06	0.06
2-3	0.45	0.23	0.43	0.17
3-4	0.99	0.99	0.99	0.91

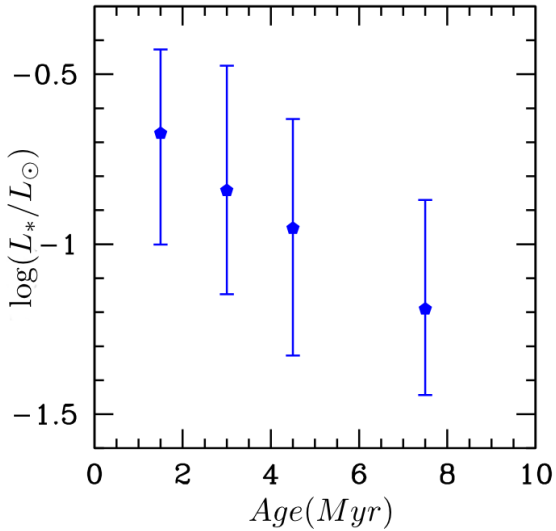


**Figure 4.** Median of the stellar luminosity (blue pentagons) for the stars in each age bin vs the age of the bin. The vertical bars represent the second and third quartiles.

to our observational sample would be to only include stars with GAIA DR2 parallaxes with relative errors  $< 20\%$  and with coherent parallaxes and proper motions, that is, within  $3 \times \sigma$  from the median value. As a test, we calculated the DCE distributions including only disk-bearing stars with coherent parallax and proper motions in each group (restricted sample), and we ob-

tained the same evolutionary trends, but with larger uncertainties, given by a larger range between the second and third quartiles. Given this result and since our goal is to make a statistical study with good significance, we will work with the initial sample without further constraints. In any case, the stars in the our observational sample have previous membership confirmation for each stellar group.

#### 2.6. Gas evolution: mass accretion rates

The mass accretion rate  $\dot{M}$  measures the amount of disk material that falls onto the star per unit time and therefore it is an indicator of the amount of gas in the disk. Different studies have shown that the mass accretion rate decreases with age (cf. Hartmann et al. 2016), which is expected from viscous evolution theories, since at the early stages the disk is fairly massive and some mechanism is responsible for the redistribution of angular momentum, allowing a fraction of the disk material to fall onto the star. Another fraction of material moves to outer radii, since angular momentum is conserved. Extensive determinations of mass accretion rates in different star forming regions have been carried out (Hartmann et al. 2016, and references therein), but they have used different methods to measure the rates. In here, we use our large sample of stellar groups at different ages to re-determine the evolution of  $\dot{M}$  in a homogeneous way.

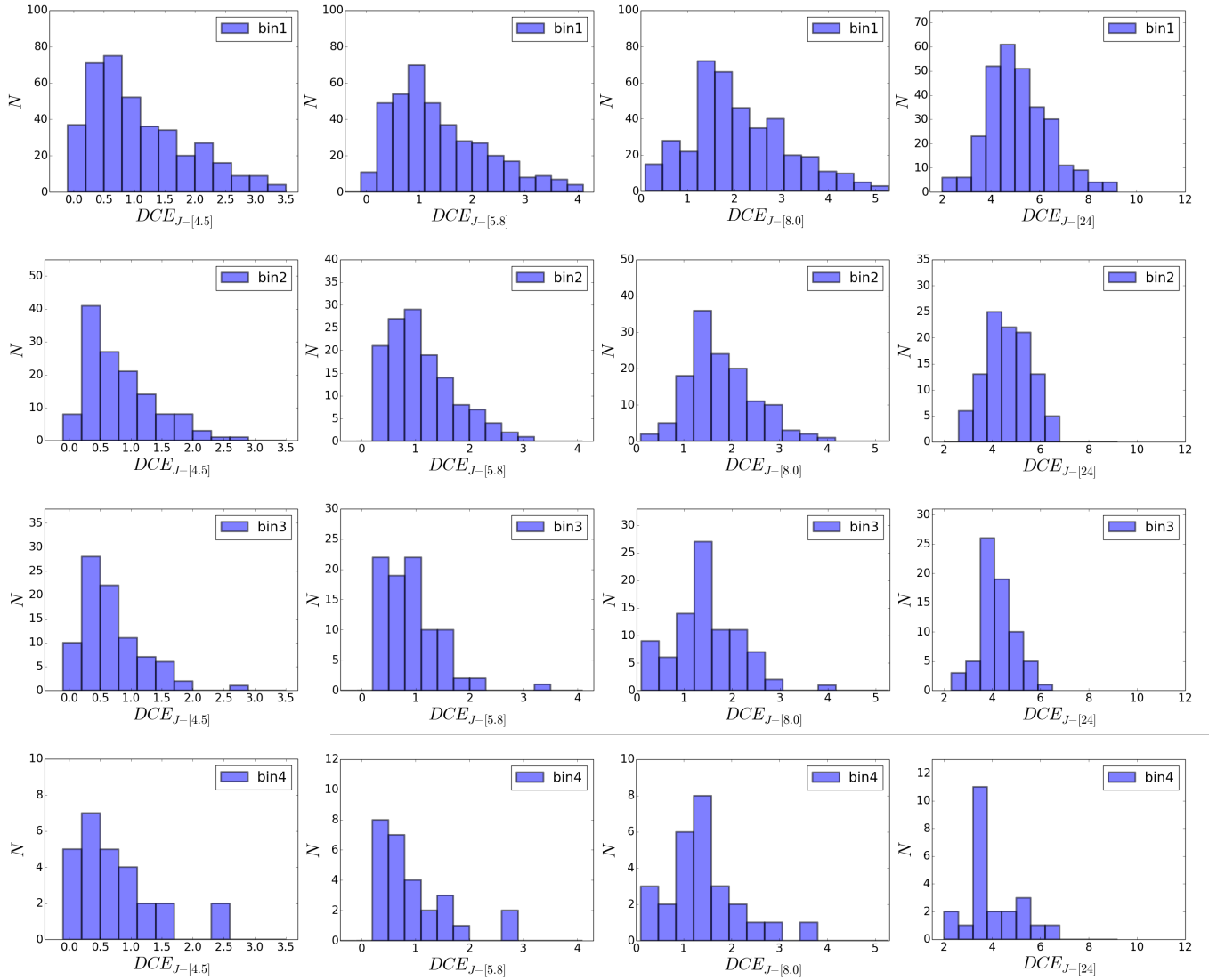


**Figure 6.** DCE distributions for: J-[4.5](first column), J-[5.8](second column), J-[8.0](third column) and J-[24](fourth column). The age of the bins increases from top to bottom.

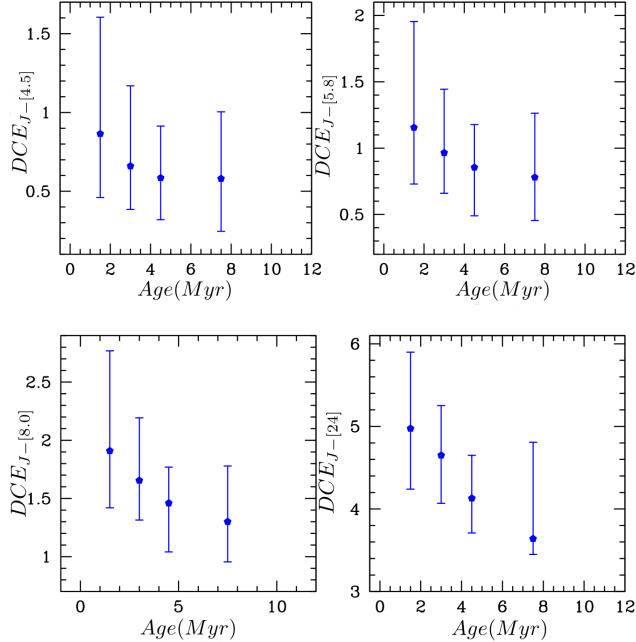


**Figure 7.** Evolution of the median disk excess for: *a*)  $J - [4.5]$  (upper left), *b*)  $J - [5.8]$  (upper right), *c*)  $J - [8.0]$  (lower left) and *d*)  $J - [24]$  (lower right). The blue pentagons correspond to the median of each distribution for each age bin and the bars are the quartiles, which indicate the range where 50% of the stars with excess are located.

### 2.6.1. Determination of mass accretion rates

We determine  $\dot{M}$  in our samples using the EW  $H\alpha$  estimated using the SpTClass tool (Hernández et al. 2007b, 2014; Hernandez et al. 2017). This estimation can be a good proxy to study the global evolution of the gas component of protoplanetary disks in young stellar objects (Ingleby et al. 2011; Alcalá et al. 2014; Maucó et al. 2016; Fairlamb et al. 2017). As discussed in §2.1, the sample used to determine  $\dot{M}$  includes some TTSs with measurements of EW  $H\alpha$  without IRAC photometry, and thus it is different from the sample analyzed in §2.5. Additionally, the stars in this sample have GAIA DR2 parallaxes, with uncertainties below 20%. Following the classification scheme from Briceño et al. (2019), we determine  $\dot{M}$  for Classical TTSs (CTTSs) and for TTSs with EW  $H\alpha$  intermediate between that of a CTTS and WTTSs (CWTTSS). Thus, we have included the following samples of CTTSs and CWTTSSs (hereafter accretors) which have stellar masses estimated following §2.2.

- *Bin 1*: We have included 228 accretors located in the ONC (§2.1.1) and 16 accretors located in Taurus (§2.1.2). Out of 244 accretors, 163 and 14 stars also belong to the sample used to study the dust in §2.5, in

the ONC and in Taurus, respectively.

- *Bin 2*: We have included 40 accretors located in the  $\sigma$  Ori cluster (§2.1.4). Out of 40 accretors, 36 stars also belong to the sample used to study the dust in §2.5.

- *Bin 3*: We have included 59 accretors located in Orion OB1b (§2.1.6). Out of 59 accretors, 19 stars also belong to the sample used to study the dust in §2.5.

- *Bin 4*: We have included 77 accretors located in Orion OB1a. (§2.1.9). Out of 77 accretors, 9 stars also belong to the sample used to study the dust in §2.5.

The  $\dot{M}$  was estimated from the  $H\alpha$  line luminosity ( $L_{H\alpha}$ ) using  $L_{H\alpha} = 4\pi d^2 \times (\text{EW } H\alpha) \times F_{cont}$ , where  $d$  is the distance calculated as the inverse of the GAIA DR2 parallaxes. The continuum flux at  $0.6563 \mu\text{m}$  ( $F_{cont}$ ) was estimated as follows. We calculated the V and  $I_c$  magnitudes of each object from the intrinsic  $[V - I_c]$  colors from Table 6 of Pecaut & Mamajek (2013) and the  $J$  magnitude corrected by extinction. The V and  $I_c$  magnitudes were converted to fluxes using the respective zero points for each filter, and  $F_{cont}$  was obtained by interpolating between these fluxes at  $0.6563 \mu\text{m}$ .

The accretion luminosity,  $L_{acc}$ , was computed using equation (10) from Ingleby et al. (2013)

$$\log(L_{acc}) = 1.0(\pm 0.2) \log(L_{H\alpha}) + 1.3(\pm 0.7), \quad (3)$$

and the mass accretion rate for each star was then obtained from the accretion luminosity using the relation  $L_{acc} = GM_* \dot{M} / R_*$ , where the derived stellar mass and radius estimated from the effective temperature and the stellar luminosity (§2.2) are used. Table 4 shows the groups for which the mass accretion rates were determined, their age, the median of  $\log(\dot{M})$  and the standard deviation  $\sigma$ , including the stars with and without IRAC photometry. In Table 8 we show all the stars with  $\dot{M}$  shown in Table 4, as well as the stars used in the determination of the different DCEs (§2.5) without EW  $H\alpha$ . The errors associated with the different DCEs in Table 8 are underestimated, since they do not include the uncertainties from the determination of spectral types, intrinsic colors or extinctions. We cannot include the propagated uncertainties, since most of the references from which the spectral types of effective temperatures were taken do not include such errors in the published data. These underestimated errors do not affect our results since we do not use them in any way as a weight to determine the disk parameters.

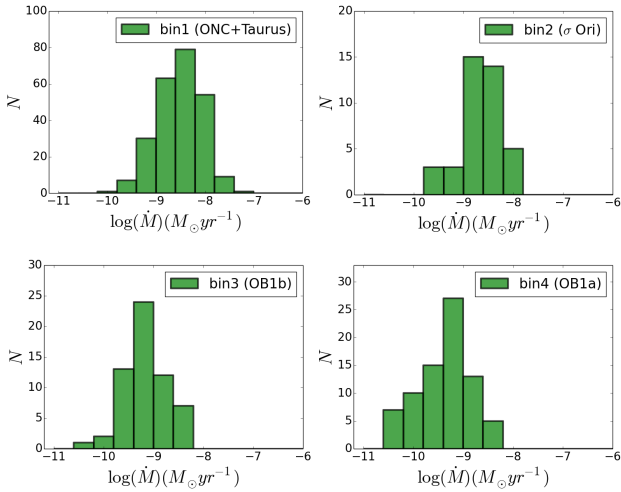
### 2.6.2. Results: the evolution of the mass accretion rate

In Figure 8 we show the distribution of mass accretion rates of each age bin. It can be seen that the distributions, and their peaks, move towards lower values as

**Table 4.** Sample for mass accretion rates

Group	Age	Stars with	Median $\log(\dot{M})$	$\sigma$	Age
	Myr	$\dot{M}$	$M_{\odot}/yr$		bin
ONC+Taurus	1-3	244	-8.49	0.50	1
$\sigma$ Ori	3	40	-8.60	0.32	2
Ori OB1b	5	59	-9.19	0.43	3
Ori OB1a	9-14	77	-9.29	0.50	4

the age of the group increases. Figure 8 confirms what has been previously discussed and found in other works (e.g. Hartmann et al. 2016). The mass accretion rates in this work were determined self-consistently using the same method for each stellar group. This is important because our results are not affected by any bias that might be introduced when different methods are used. Figure 9 shows the median of the mass accretion rates vs the age bin. The bars are the quartiles, which show where 50% of the data of each age bin lie. There is a clear trend of decreasing accretion rates with age, as previously found. The median seems to fall more rapidly during the first 5 Myrs, and then the decrease flattens out. Similar behavior is observed in the evolution of the medians of the different DCEs (see Figure 7).

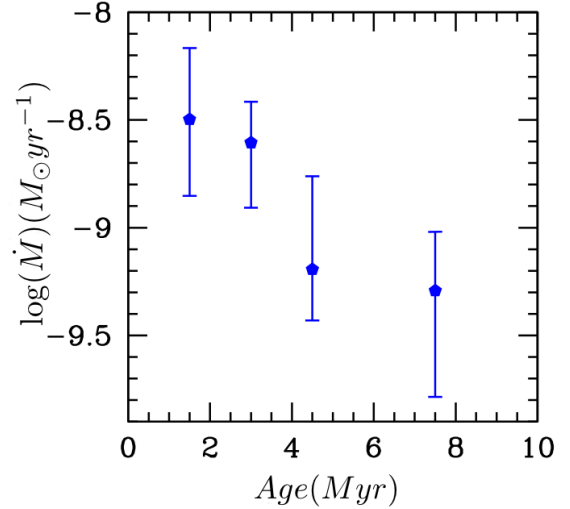
**Figure 8.** Mass accretion rates distributions calculated in this work, for the different age bins.

### 3. INTERPRETATION OF OBSERVED EVOLUTION

#### 3.1. Evolutionary models

##### 3.1.1. Mass accretion rates in viscously evolving disks

We use the similarity solution of Lynden-Bell & Pringle (1974) of a disk radial viscous evolution for the case of a power-law radial dependence of the viscosity coefficient. In particular, for a viscosity that increases linearly with

**Figure 9.** Median of the mass accretion rates for the different age bins. The blue bars are the quartiles, which show where 50% of the data of each age bin lie.

radius,  $\nu \propto R$ , the surface density distribution as a function of time  $t$  can be written as

$$\Sigma(R, t) = \frac{M_d(0)}{2\pi R_1^2} \frac{1}{r \mathbb{T}^{3/2}} \exp\left[-\frac{r}{\mathbb{T}}\right], \quad (4)$$

the mass accretion rate at  $R = 0$  as

$$\dot{M}(0, t) = \frac{M_d(0)}{2t_s} \frac{1}{\mathbb{T}^{3/2}}, \quad (5)$$

and the disk mass as

$$M_d(R, t) = \frac{M_d(0)}{\mathbb{T}^{1/2}} \left\{ 1 - \exp\left[-\frac{r}{\mathbb{T}}\right] \right\} \quad (6)$$

(Hartmann et al. 1998). Here,  $M_d(0)$  is the initial disk mass,  $R_1$  is a characteristic radius, inside which 60% of the original disk mass is located,  $r = R/R_1$ , and  $\mathbb{T} = t/t_s + 1$  is a non-dimensional time, where  $t_s = R_1^2/(3\nu_1)$  is the characteristic viscous timescale at  $R_1$ , and  $\nu_1$  is the viscosity at  $R_1$ .

In the Shakura & Sunyaev (1973) prescription, the viscosity is given by  $\nu = \alpha c_s H$ , where  $H = c_s/\Omega_K$  is



the scale height,  $\Omega_K = (GM_*/R^3)^{1/2}$  is the Keplerian angular velocity, where  $G$  is the gravitational constant and  $M_*$  is the stellar mass,  $c_s = (kT/\mu m_H)^{1/2}$  is the sound speed, where  $T$  is the temperature,  $\mu = 2.34$  is the mean molecular weight,  $k$  is the Boltzmann constant,  $m_H$  is the hydrogen mass, and  $\alpha$  is a free parameter.

Using this prescription, the viscosity is  $\nu \propto \alpha T R^{3/2}$ . For an irradiated disk, and  $R \gg R_*$ ,  $T \propto R^{-1/2}$  in which case  $\nu \propto R$  and the similarity solution can be applied (cf. Hartmann et al. 1998). Following this work, we assume that this viscosity law holds at each radius and use equation (4) to describe the evolution of the disk surface density distribution.

Using the  $\alpha$  viscosity prescription and equation (5), the mass accretion rate onto the star can be written as

$$\dot{M}(0, t) = \frac{3\alpha}{2(GM_*R_1)^{1/2}} \frac{kT_1}{\mu m_H} \frac{M_d(0)}{\mathbb{T}^{3/2}}, \quad (7)$$

for a temperature profile  $T = T_1(R/R_1)^{-1/2}$ , such that the viscous time is  $t_s = (1/3\alpha)(GM_*R_1)^{1/2}(\mu m_H)/(kT_1)$ . For a given initial disk mass  $M_d(0)$  and a characteristic radius  $R_1$ , and for a star of mass  $M_*$ , equation (7) gives the predicted evolution of the mass accretion rate onto the star. Since for the stellar groups discussed in §2.1,  $t \gg t_s$ , one obtains

$$\dot{M}(0, t) = \frac{(GM_*R_1)^{1/4}}{2(3\alpha)^{1/2}} \left(\frac{\mu m_H}{kT_1}\right)^{1/2} \frac{M_d(0)}{t^{3/2}}. \quad (8)$$

We adopt the approximation  $T_1 = T_{d2}(100 \text{ au}/R_1)^{1/2}$ , with  $T_{d2} = 10\text{K}$ , a typical temperature at 100 AU (cf. D'Alessio et al. 1998, 2001). Then, the mass accretion rate can be written as

$$\frac{\dot{M}(0, t)}{M_\odot \text{ yr}^{-1}} = 1.39 \times 10^{-8} \left(\frac{\alpha}{0.01}\right)^{-1/2} \left(\frac{M_*}{M_\odot}\right)^{1/4} \left(\frac{R_1}{\text{AU}}\right)^{1/2} \times \left(\frac{T_{d2}}{10\text{K}}\right)^{-1/2} \left(\frac{M_d(0)}{M_\odot}\right)^{-3/2} \left(\frac{t}{\text{Myr}}\right)^{-3/2}. \quad (9)$$

In the fiducial model of Hartmann et al. (1998), the parameters  $M_d(0)$  and  $R_1$  were set to  $0.1 M_\odot$  and 10 au, respectively, and calculations were shown for  $M_* = 0.5 M_\odot$ . In here, we will use the values for  $\alpha$ ,  $M_d(0)$ ,  $R_1$ , and  $M_*$ , that are consistent with our observational samples and the observed decay of mass accretion rate with age (cf. Figure 9).

We adopt a stellar mass  $M_* = 0.30 M_\odot$ , which corresponds to the mean stellar mass from our sample (see §2.4), as representative of the evolution of the mean color excesses. We fit the observed decay of the mass accretion rate with age (Fig. 9) using equation (9) and find the triads of values  $(R_1, M_d(0), \alpha)$  that provide the best  $\chi^2$  fit to the data.

Figure 10 shows the goodness of the fits, as indicated by the value of  $\chi^2$ , for a range of values of  $R_1$  and  $M_d(0)$ , and for three values of  $\alpha$ : 0.01, 0.001, and 0.0001.

The lowest value of  $M_d(0)$  among the best fitting models for  $\alpha=0.001$  is about  $0.03 M_\odot$ , or about twice the minimum solar nebula (MMSN). The mean value of the disk mass for disks in the 2 Myr old Taurus association is  $0.005 M_\odot$  (Andrews & Williams 2005), so in principle the mean initial disk mass could be lower than  $0.03 M_\odot$ . However, Andrews & Williams (2005) note that the formation of giant planets requires disk masses of a few MMSN. In addition, models with  $\alpha \lesssim 0.001$  predict very low values of  $R_1$ , less than 5 au. In contrast, a large ALMA disks' survey in Orion finds that Class 0 and Class I objects have mean dust disk radii of  $\sim 45$  au and  $\sim 37$  au, respectively (Tobin et al. 2020). These objects are representative of the initial stages of viscous evolution, which argues against very low values of  $R_1$ .

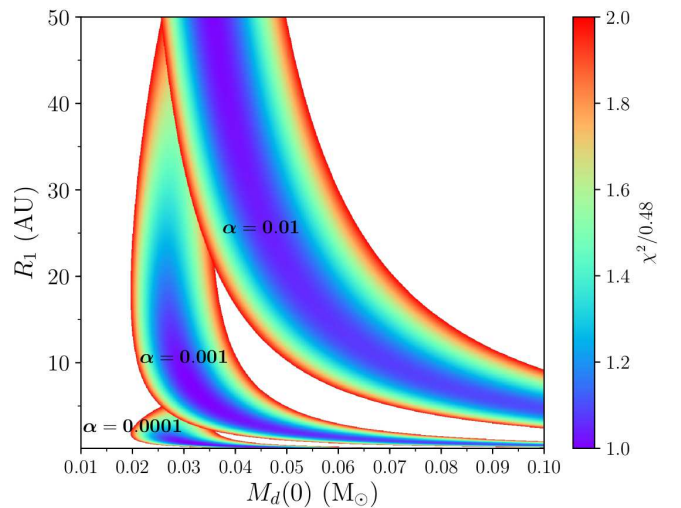


**Figure 10.** Normalized  $\chi^2/0.48$  for the fits to the observed decay of mass accretion rate with age in Figure 9 from different combinations of the evolutionary parameters  $R_1$  and  $M_d(0)$ , and the viscosity parameter  $\alpha$ . Each color map region corresponds to a different value of  $\alpha$ , indicated in the label. The values are normalized to the global minimum as indicated in the scale.

For  $\alpha = 0.01$ , Figure 10 shows that values of  $R_1$  ranging from  $\sim 5$  au to radii even larger than 50 au, with  $0.03 M_\odot \lesssim M_d(0) \lesssim 0.1 M_\odot$ , give reasonable fits to the observed data (cf. Figure 11). The observed mean values of the dust disks' radii for Class 0 and Class I objects from Tobin et al. (2020), suggest that the characteristic radius  $R_1$  is larger than the values inferred from the analysis for  $\alpha = 0.001$  and 0.0001. To be consistent with these considerations, we adopt models with  $\alpha = 0.01$ .

Figure 11 shows the median values of the mass accretion rate distributions at each age bin (also shown in Figure 9 and Table 4). The standard deviation of

the distributions of mass accretion rates (shown with the error bars) was calculated using the median absolute deviation (MAD) of the observational data, assuming Gaussian distributions, with the relation  $\sigma = 1.4826 \text{ MAD}$ . The red shaded area in Figure 11 corresponds to the mass accretion rates predicted by triads of values  $(R_1, M_d(0), \alpha)$  which have normalized  $\chi^2/0.48 \leq 2$  in Figure 10, and the green solid line shows the theoretical mass accretion rate for one of these triads,  $R_1 = 10$  au (e.g. Hartmann et al. 1998),  $M_d(0) = 0.07 M_\odot$ , and  $\alpha=0.01$ . This analysis suggests that the observed decay of  $\dot{M}$  with age is consistent with viscous evolution of the gas in the disk, for these evolutionary models.

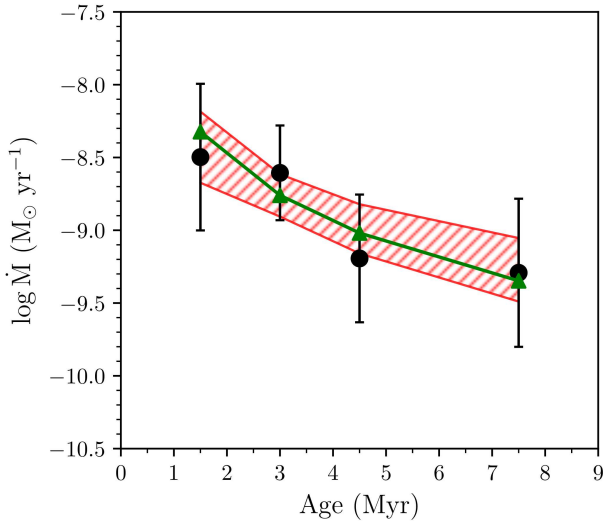


**Figure 11.** Median mass accretion rates as a function of age (black points), where the error bars correspond to the standard deviation of the distributions at each age. The solid green line shows the theoretical mass accretion rate for  $M_d(0) = 0.07 M_\odot$ ,  $R_1 = 10$  au, and  $\alpha=0.01$ . The red region corresponds to models with  $\chi^2/0.48 \leq 2$  in Figure 10.

### 3.1.2. D’Alessio Models

We aim to calculate the emission of disks for which the radial distribution of surface density is given by equation (4) at each one of the age bins for which we have obtained color excesses. To do so, we need to calculate the vertical structure of the disk, namely, we need to solve the disk structure equations to obtain the radial and vertical distribution of the temperature and volumetric density which result in the given  $\Sigma(R, t)$ . For this purpose, we use the irradiated disk models developed by D’Alessio (1996), D’Alessio et al. (1998, 1999, 2001, 2006), adopting several approximations to adapt these models to the Lynden-Bell & Pringle (1974) models.

The D’Alessio models assume that the disk is steady, geometrically thin and axially symmetric. The dust and gas are assumed to be thermally coupled. The disk is heated by absorption of stellar and accretion shock radiation as well as viscous dissipation, and it is cooled by dust emission. The viscosity is given by the Shakura & Sunyaev (1973) prescription.

As discussed, with this prescription the viscosity only increases linearly with radius, as assumed in the Lynden-Bell & Pringle (1974) similarity solution, if the temperature depends on radius as  $T \propto 1/R^{1/2}$  (Hartmann et al. 1998), which only happens approximately in more realistic physical situations (cf. D’Alessio et al. 2001, 2006). Nonetheless, we will adopt the  $\alpha$  prescription to represent the viscosity, with the sound speed evaluated at the midplane temperature.

Another issue is that in the D’Alessio models the surface density is that of a steady disk and lacks the exponential fall-off at large radii (cf. equation 4). Following Qi et al. (2011), we modified the  $\alpha$  parameter so that  $\alpha = \alpha_0 e^{R/R_t}$ , where  $R_t$  is the critical radius outside which the exponential fall-off becomes important and  $\alpha_0$  is the value of  $\alpha$  at  $R \ll R_t$ . The critical radius is given by  $R_t = R_1 \mathbb{T}$  (equation 4). For  $t \gg t_s$ , this is

$$R_t = 1.37 \times 10^2 \text{ AU} \left( \frac{T_{d2}}{10 \text{ K}} \right) \left( \frac{M_*}{0.30 M_\odot} \right)^{-1/2} \left( \frac{\alpha_1}{0.01} \right) \left( \frac{t}{\text{Myr}} \right). \quad (10)$$

As stated in Qi et al. (2011), this modification adds an exponential taper to the radial distribution of the surface density, and does not reproduce the predicted behavior of the mass flow at large radii, but the effect on the observables is negligible, since irradiation dominates over viscous heating at these large radii.

The main input parameters for the D’Alessio models are the stellar mass, radius, and effective temperature, the mass accretion rate and viscosity parameter, the dust composition, size distribution, and spatial distribution in the disk. To be consistent with the surface density distribution resultant from viscous evolution calculations at a given age bin (equation 4), the model uses as further input the transition radius  $R_t$ , equation (10), with  $\alpha = 0.01$ .

In addition, we use the evolutionary models of Siess et al. (2000) for a star of mass  $0.30 M_\odot$  (§2.4 and §3.1.1) to obtain the stellar luminosity and effective temperature at each age bin (see Table 5).

In the models, the disks are irradiated by the star and the accretion shocks on the stellar surface. The shocks are formed when disk material falls onto the star, creating hot spots on the surface, with a characteristic temperature of  $\sim 8000 \text{ K}$  (Hartmann et al. 2016). The total luminosity irradiating the disk is then  $L_t = L_* + L_{\text{shock}}$ , where we adopt  $L_{\text{shock}} = L_{\text{acc}} = GM_* \dot{M} / R_*$ .

The dust species used in the models are silicates and graphite, with abundances typical of the ISM (Draine & Lee 1984). We assume a power law size distribution for the grain sizes, with exponent 3.5, between a minimum grain radius  $a_{\min} = 0.005 \mu\text{m}$  and a maximum radius  $a_{\max}$ . Dust settling is included in the models by assuming two populations of dust grains with different values of  $a_{\max}$ . The disk upper layers contain small grains, while the large grains are concentrated towards the midplane (D’Alessio et al. 2006). We use  $a_{\max} = 0.25 \mu\text{m}$  for the upper layers, and  $a_{\max} = 1 \text{mm}$  in the midplane (D’Alessio et al. 2006). Both populations have different dust-to-gas mass ratios,  $\zeta$ . Because the midplane region contains the mass of the dust grains that have settled from the upper layers, the corresponding  $\zeta_{\text{big}}$  is larger than the standard value  $\zeta_{\text{std}}=0.01$  (Draine & Lee 1984). Correspondingly, in the surface layers  $\zeta_{\text{small}}$  is smaller than the standard value. The large grain population extends to a height  $z_{\text{big}}(r)$ , and we choose  $z_{\text{big}}(r) = H$  in this work, where  $H$  is the scale height at the local temperature. The degree of dust settling is quantified using the parameter  $\epsilon = \zeta_{\text{small}}/\zeta_{\text{std}}$  (D’Alessio et al. 2006). The values for  $\zeta_{\text{big}}/\zeta_{\text{std}}$  are computed using equation (A5) from D’Alessio et al. (2006).

The disk structure is calculated self-consistently by solving the vertical structure equations in an iterative scheme (D’Alessio et al. 1998). The radiative transfer is done using mean opacities calculated in two wavelength regions, the “stellar” and the “local” temperature regions (Calvet et al. 1991; D’Alessio et al. 1998). The mean opacities are computed from the monochromatic opacities of each dust species. The “stellar” mean opacities are the average of opacities calculated at the stellar and shock temperatures, weighted by the corresponding luminosity.

Once the disk structure is computed, the emission from the disk for a given inclination angle  $i$  is calculated with a ray-by-ray solution of the transfer equation, including thermal emission from the dust and a single scattering of stellar radiation (D’Alessio et al. 1998, 2006).

The most important contributor to the overall disk emission in the near-IR is the disk region at the dust destruction radius (Isella & Natta 2005; D’Alessio et al. 2005; Dullemond & Monnier 2010), which we name “the wall”. For radii smaller than the wall radius the temperature reaches values above the silicates sublimation temperature ( $\sim 1500 \text{K}$ ), and we assume that dust does not exist. The wall is generally assumed to be vertical and irradiated frontally by the central star, but several studies have shown that the wall may instead be curved (Isella & Natta 2005; Tannirkulam et al. 2008; McClure et al. 2013). This kind of shape for the wall is expected because the larger dust grains settle towards the disk midplane; since the micron-sized atmospheric grains are more efficient absorbing stellar radiation, the larger grains can survive closer to the star. In addition, the sublimation temperature decreases with den-

sity (Pollack et al. 1994). McClure et al. (2013) modeled the SED and near-IR spectra of four T Tauri stars in the Taurus region and found that a treatment of the wall that accounts for its curvature allows for a much better fit to the spectra than a vertical wall. Following McClure et al. (2013) we mimic the curvature of the wall as a two-layer wall. The lower layer contains larger ( $1 \mu\text{m}$ ) hotter grains (1500 K), while the upper layer contains sub-micron ( $0.25 \mu\text{m}$ ), cooler (1000 K) grains. The radius of each layer,  $R_{in1}$  and  $R_{in2}$  for the lower and upper wall, respectively, is set by the total luminosity,  $L_t$ , and the respective dust properties, using the relation  $R_{in_i} \propto (L_* + L_{\text{acc}})^{1/2} (T_{w_i})^{-2}$ , where  $T_{w_i}$  is the sublimation temperature of the dust grains in the lower ( $i = 1$ ) and the upper ( $i = 2$ ) wall, respectively. Both layers are frontally illuminated with a normal impinging angle. The calculation of the emission from each layer follows the treatment of D’Alessio et al. (2005).

The total SED is constructed by adding the emission from the disk, the wall, the star, and the accretion shock. We assume the shock emits as a blackbody with  $T = 8000 \text{K}$  and emitting area  $f4\pi R_*^2$ . The filling factor  $f$  is then calculated by the condition that the shock luminosity is the accretion luminosity.

### 3.2. Comparison with observations

With gas evolution constrained by the observations of mass accretion rates onto the star at different ages (§2.6.2), we aim to find the dust properties that better describe the observed evolution of the disk color excesses (§2.5). Specifically, we constructed grids of disk models at each age bin and calculated the SEDs and color excesses for each model in the grids (§3.2.1). We used the models’ color excesses to estimate the distributions of the degree of dust settling and of the inner wall height that best fitted the observed distribution of color excesses at each age.

#### 3.2.1. Construction of the model grid

Using the methods described in Section 3.1.2, we computed a grid of disk models for each age bin. Models were calculated using the following mass accretion rates:  $2 \times 10^{-8}, 1 \times 10^{-8}, 5 \times 10^{-9}, 1 \times 10^{-9}$  and  $5 \times 10^{-10} M_{\odot} \text{yr}^{-1}$ . For simplicity, we only considered cases where the upper and the lower parts of the two-layered wall at the dust destruction radius have the same ratio  $z_{\text{wall}}/H = z_{\text{wall}1}/H_1 = z_{\text{wall}2}/H_2$ , where  $H_1$  and  $H_2$  are the gas scale heights  $H_1 \propto T_{w_1}^{1/2} R_{in1}^{3/2} M_*^{-1/2}$  and  $H_2 \propto T_{w_2}^{1/2} R_{in2}^{3/2} M_*^{-1/2}$  at the lower and upper wall, respectively.

As mentioned before, we assume that the dust in the lower and upper wall sublimates at  $T_{w_1} = 1500 \text{K}$  (with  $a_{\max} = 1 \mu\text{m}$ ) and  $T_{w_2} = 1000 \text{K}$  (with  $a_{\max} = 0.25 \mu\text{m}$ ), respectively. We run models with values for  $z_{\text{wall}}/H$  from 0.1 to 4, in steps of 0.8. The total physical height of this two-layered wall is then

**Table 5.** Parameter of the models

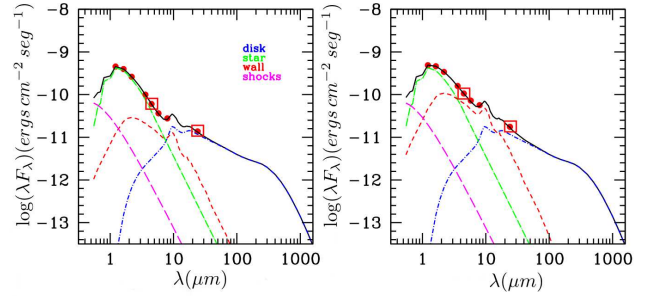
Age	$R_*$	$T_{\text{eff}}$	$L_*$	$R_{\text{disk}}$
Myr	$R_{\odot}$	$K$	$L_{\odot}$	au
1.5	1.71	3360	0.38	230
2.5	1.25	3385	0.21	410
4.5	0.97	3416	0.13	660
7.5	0.79	3451	0.09	1080

$Z_{\text{wall}}(\text{au}) = (z_{\text{wall}}/H)(H_1 + H_2)$ . We also varied the settling parameter  $\epsilon$  (from 1 to 0.0001), and cosine of the inclination  $\cos(i)$  (from 0 to 1). For each age bin we run 1350 disk models, thus the total number of models calculated, including the four bins, is 5400. Table 5 shows the parameters of the models, adopted in each age bin. Since we are not including nor modeling data beyond  $24 \mu\text{m}$ , the disk outer radius  $R_{\text{disk}}$  is chosen arbitrarily, such that it is located beyond the critical radius  $R_t$ . We use these parameters to compute disk models and build their synthetic SEDs and DCEs (see Figures 12 and 13).

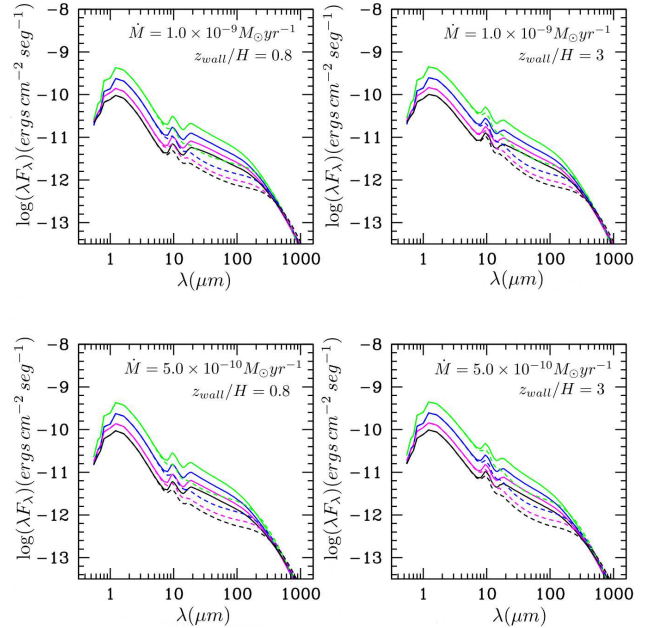
To compute the DCEs of the models in the IRAC and MIPS 24 bands we calculate their fluxes and magnitudes in the 2MASS, IRAC and MIPS 24 bands, using the corresponding transmission profiles of the filters. Using the  $J$  band and the IRAC and MIPS 24 bands, we then built the corresponding synthetic colors. We also obtain the values for the photospheric magnitudes and photospheric colors of the models, and calculate the corresponding DCEs, by subtracting the models' photospheric colors from the colors obtained from the complete synthetic SED of the model. We calculate the DCEs for the colors  $J$ -[4.5],  $J$ -[5.8],  $J$ -[8.0] and  $J$ -[24].

Figure 12 shows the SEDs of disk models with stellar parameters from bin 1, for  $z_{\text{wall}}/H = 0.8$  (left panel) and  $z_{\text{wall}}/H = 3$  (right panel). It can be seen that at  $24 \mu\text{m}$  the flux is dominated by the disk contribution. Accordingly, the excess at  $24 \mu\text{m}$  can be used to estimate the degree of dust settling in the disk, quantified by the parameter  $\epsilon$  (§3.1.2), which measures the dust depletion in the disk upper layers (D'Alessio et al. 2006). In Figure 13 we show the SEDs of disk models with  $z_{\text{wall}}/H = 0.8$  (left panels) and  $z_{\text{wall}}/H = 3$  (right panels), for bin 1 (green), bin 2 (blue), bin 3 (magenta), and bin 4 (black). In the upper and lower panels we show models with  $\dot{M} = 1.0 \times 10^{-9} M_{\odot}/\text{yr}$  and  $\dot{M} = 5.0 \times 10^{-10} M_{\odot}/\text{yr}$ , respectively; additionally, two values of the parameter  $\epsilon$  are indicated with different lines: 0.01 (solid lines) and 0.0001 (dashed lines).

In Figure 14 we plot the  $DCE_{J-[4.5]}$  vs  $DCE_{J-[24]}$  from the corresponding grid of disk models used in each age bin (empty circles), showing in different colors various values of  $\epsilon$ : 0.1 (blue), 0.01 (red), 0.001 (green)



**Figure 12.** SEDs of disk models from bin 1, with  $\epsilon=0.0001$ ,  $z_{\text{wall}}/H=0.8$  (left) and  $z_{\text{wall}}/H=3$  (right), with  $\dot{M} = 1.0 \times 10^{-9} M_{\odot}/\text{yr}$ . Each line represents a different component: the star (green dashed), the wall (red short-dashed), the accretion shocks (pink long-dashed), the disk (blue dot-dashed), and the total (black solid). The red points correspond to the 2MASS, IRAC, and MIPS 24 fluxes; the red squares indicate the flux at  $4.5 \mu\text{m}$  and at  $24 \mu\text{m}$ . The inclination is  $\cos(i) = 0.5$ .



**Figure 13.** SEDs of disk models for different age bins: bin 1 (green), bin 2 (blue), bin 3 (magenta), and bin 4 (black), with  $\dot{M} = 1.0 \times 10^{-9} M_{\odot}/\text{yr}$  (upper panels) and  $\dot{M} = 5.0 \times 10^{-10} M_{\odot}/\text{yr}$  (lower panels). Two values of  $\epsilon$  are shown: 0.01 (solid lines) and 0.0001 (dashed lines). The left and right panels correspond to models with  $z_{\text{wall}}/H=0.8$  and  $z_{\text{wall}}/H=3$ , respectively. The inclination is  $\cos(i) = 0.5$ .

and 0.0001 (magenta). We also plot the observational sample in each bin (black solid triangles) for reference. Both the observational data and the models locate in



the same region. The models with the largest  $DCEs$  (e.g.  $DCE_{J-[4.5]} \gtrsim 3.5$  and  $DCE_{J-[24]} \gtrsim 8$ ) correspond to models of highly inclined disks, which are more difficult to detect and observe. Notice that, as the age of the bin increases, the observed disks move towards the smallest values of  $\epsilon$ , which is in agreement with the results we find using approximate Bayesian computation (see §3.2.3).

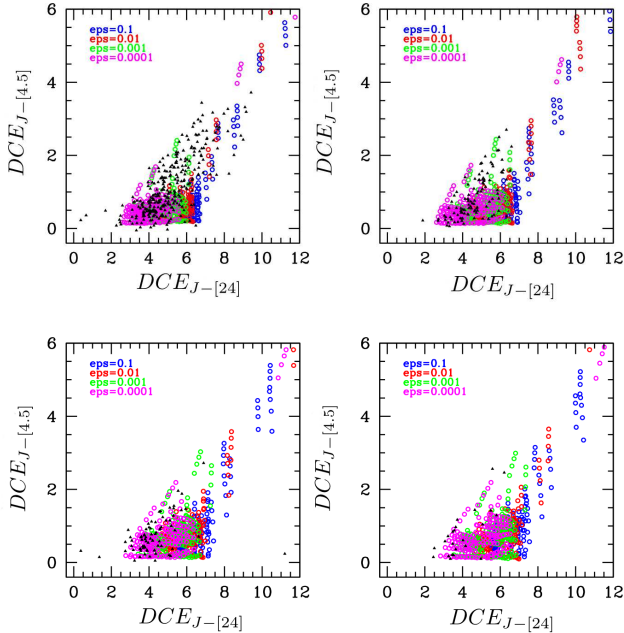


**Figure 14.** Synthetic DCEs obtained from the grid of models for bin 1 (upper left), bin 2 (upper right), bin 3 (lower left) and bin 4 (lower right). Various  $\epsilon$  are shown in different colors: 0.1 (blue), 0.01 (red), 0.001 (green) and 0.0001 (magenta). The observational sample in each age bin (black triangles) is shown for comparison.

### 3.2.2. Spatial distribution of dust: forward modeling

In the previous Section 3.1 we used a model to define a sampling of disk DCEs for each age bin. Our observed data comprise distributions of DCEs as shown in Figure 6. Our goal then is to take our grid of models and determine the underlying parameter values which would recreate the observed DCE histograms. We will use approximate Bayesian computation (ABC) to quantify the posterior probability distributions for each parameter.

ABC was developed as a way to apply Bayesian statistical methods when an analytical representation of the data likelihood function is replaced with simulation-based models (Turner & Van Zandt 2012). When using ABC, the forward model grid allows us to sample directly from the posterior by generating simulated datasets that match the observations. ABC requires a forward model, a summary statistic to use on the data

and on the simulations, and a rule-set to accept or reject the choice of parameters. The Bayesian prior is defined by the parameters used in the precalculated grid discussion in §3.2.1. The summary statistic that we use is the histogram representations of the data presented in §2.5 (see Figure 6). We use a simple but strict rejection policy where the forward modeled simulation of the data must match our observed histograms precisely (Marjoram et al. 2015).

In practice, we search for the distributions of the input parameters  $\log(\epsilon)$  and  $z_{wall}/H$  (see definition in §3.2.1) that best reproduce the observations. We create a realization of the observed histograms by sampling from the cumulative distributions of the input parameters  $\log \dot{M}$ ,  $\cos i$  and either  $\log \epsilon$  or  $z_{wall}/H$ , depending on the color excess we aim to reproduce, and calculating the color excess for the given combination of model parameters. We carried out 100 such realizations, each resulting on a distribution of input parameters that fitted the observations. We use the distributions for all realizations to calculate a mean value and standard deviation at each bin of the distribution for each of our parameters of interest. To calculate the cumulative distributions of input parameters, we used the observed mass accretion rate distributions in each age bin (§2.6.1) and assumed a uniform distribution of inclinations, degrees of settling and wall heights.

Depending on the DCE we want to study and reproduce, we use different free parameters. Since the inner wall emission dominates at  $4.5 \mu m$  in the SEDs (cf. Figure 12), we use  $(z_{wall}/H, \log(\dot{M}), \cos(i))$  as the input parameters when we attempt to reproduce the DCEs in the IRAC bands ( $J-[4.5]$ ,  $J-[5.8]$  and  $J-[8.0]$ ). On the other hand, the degree of dust settling is better traced by  $24 \mu m$ , where the disk dominates the emission (cf. Figure 12), hence, we use  $(\log \epsilon, \log(\dot{M}), \cos(i))$  as input parameters when we attempt to reproduce the DCEs in the MIPS 24 band ( $J-[24]$ ).

### 3.2.3. Results

Following the method outlined in §3.2.2, we inferred the distribution of  $z_{wall}/H$  from the color excesses  $J-[4.5]$ ,  $J-[5.8]$  and  $J-[8.0]$ , and the distribution of the dust settling parameter  $\log(\epsilon)$  from the  $DCE_{J-[24]}$  at each age bin. Figure 15 shows the  $z_{wall}/H$  distributions inferred from  $DCE_{J-[4.5]}$  (left column) and the distributions of  $\log(\epsilon)$  (right column) for each age bin, the youngest located at the top row. We only show the distribution for the  $DCE_{J-[4.5]}$  since  $4.5 \mu m$  is the best band to probe the wall height (see §3.2.1 and Figure 12). The distributions for  $\log(\epsilon)$  and  $z_{wall}/H$  and their peaks move towards lower values as the age of the bin increases (from top to bottom), similarly to what is observed for the mass accretion rates (Figure 8) and DCEs (Figure 6).

Notice that we use a central star in each age bin, with the corresponding stellar properties ( $T_{eff}, R_*, L_*$ ) associ-

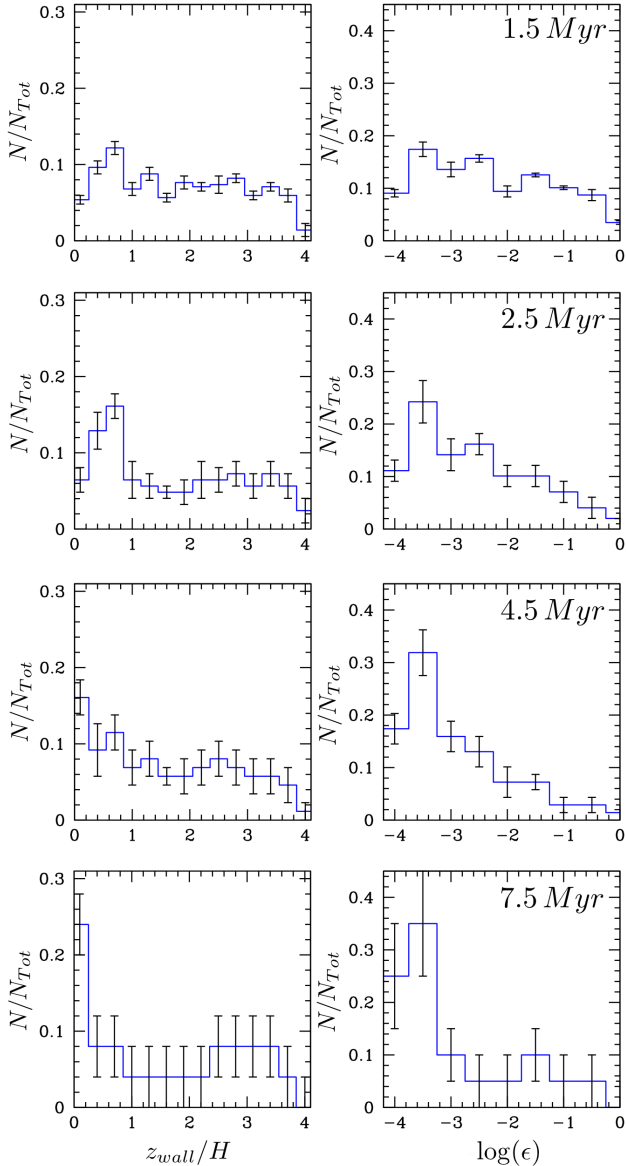


**Figure 15.** Mean distributions for  $z_{wall}/H$  (left column) and  $\log(\epsilon)$  (right column), for each age bin, with the youngest bin on the top row. The distribution of  $z_{wall}/H$  has been calculated from the color excess  $J - [4.5]$  with  $\epsilon = 0.001$  for bins 1, 2, 3 and 4. The distribution of  $\log(\epsilon)$  has been calculated from the color excess  $J - [24]$ , with  $z_{wall} = 1.5 H$ . The vertical lines are the standard deviations of each bin.

ated to the age of the bin, thus the gas scale height  $H$  at a fixed radius is different from one bin to the other. The gas scale height is  $H \propto M_*^{-1/2} R^{3/2}$ , where  $M_*$  is fixed to  $0.30 M_\odot$  (see §3.1.1) for all bins, but the dust destruction radius,  $R = R_{in}$ , moves inwards with age since the luminosity of the star is decreasing. This means that the gas scale height, and thus the wall, is physically lower as the age bin increases, since it is measured in units of  $H$ ,

which decreases with age. In order to test the robustness of the method, we increased the number of realizations (see §3.2.2) in the analysis and no changes in our results were found.

## 4. DISCUSSION

### 4.1. Implications for disk evolution

By reproducing the observed distributions of DCEs (§2.5) using an extensive grid of disk models (§3.2.1) and taking into account the observed evolution of mass accretion rates (§2.6.2), we have inferred how the distributions of the disk parameters  $\log(\epsilon)$  and  $z_{wall}/H$  (Figure 15) change with age, comparing results for the different age bins. Figure 16 shows the results of the dust evolution analysis shown in §3.2.3 in a different way. This Figure shows the median of the parameters  $z_{wall}/H$  and  $\log(\epsilon)$  vs the age of the bin, calculated from the mean and quartiles of the mean distributions in Figure 15.

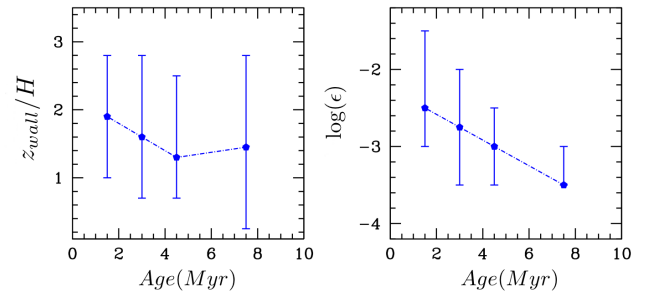


**Figure 16.** Median of  $z_{wall}/H$  (left panel) obtained from  $DCE_{J-[4.5]}$  and median of  $\log(\epsilon)$  (right panel) obtained from  $DCE_{J-[24]}$  vs the age of the bin. The error bars are the quartiles, which show where 50% of the disks lie. In the  $z_{wall}/H$  panel, we show the results for a fixed  $\epsilon: 0.001$ , and in the  $\log(\epsilon)$  panel we show the results for a fixed  $z_{wall}/H: 1.5$

The decrease of the median of  $\log(\epsilon)$  with age in the right panel in Figure 16 indicates that dust depletion increases with age in the inner disk regions. However, the region probed by the flux at  $24 \mu m$  changes as the dust gets increasingly depleted (D’Alessio et al. 2006). In Figure 17 we show the contribution to the total flux from the disk region inside radius  $R$  as a function of  $R$  at  $8 \mu m$  (blue line) and  $24 \mu m$  (green line) for disks with the median parameters in age bins 1 and 4.

It can be seen that  $\sim 90\%$  of the flux at  $24 \mu m$  arises from the inner  $\sim 10$  au of the disk at age bin 1 with  $\epsilon = 0.003$ , while the same flux fraction arises from the inner  $\sim 1$  au of the disk for age bin 4, with  $\epsilon = 0.0003$ . In both cases, we are probing the inner few au of the disk ( $\sim 1 - 10$  au), which is the region where terrestrial planets form.

The low values of  $\log(\epsilon)$  in Figure 15, (right panels) indicate that even for the youngest groups, disks al-

ready show significant dust settling, suggesting that the settling process starts at very early evolutionary stages ( $\sim 1$  Myr).

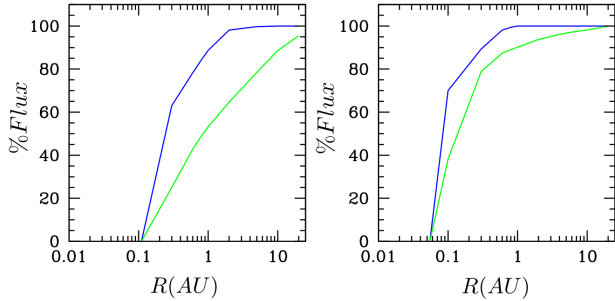


**Figure 17.** Emergent flux at  $8 \mu\text{m}$  (blue line) and  $24 \mu\text{m}$  (green line), at different disk radii, for a disk with  $\log(\dot{M}) = -8.49 M_{\odot}/\text{yr}$  with  $\epsilon = 0.003$  (left panel) and  $\log(\dot{M}) = -9.29 M_{\odot}/\text{yr}$  with  $\epsilon = 0.0003$  (right panel), for a 1.5 (bin 1) and 7.5 Myr old (bin 4) star, respectively.

Our results support the conclusions derived from analysis of IRS spectra in Taurus (Furlan et al. 2006, 2009), Ophiuchus (McClure et al. 2010), and Chamaeleon (Manoj et al. 2011). Furlan et al. (2009) find values of  $\log(\epsilon) \sim -2$  to  $-3$  in Taurus, Chamaeleon I (2 Myr; Luhman 2004) and Ophiuchus ( $< 1$  Myr; Luhman & Rieke 1999). These values are consistent with the median of  $\log(\epsilon)$  shown in Figure 16 for bin 1 and 2, indicating a large degree of settling in disks. Similarly, our results are consistent with the results of the analysis of Herschel/PACS data of disks in the (1.5 Myr) Lynds 1641 region by Grant et al. (2018) and in the (3 Myr)  $\sigma$  Ori cluster by Maucó et al. (2016), who found a significant fraction of disks with  $-2.8 \lesssim \log(\epsilon) \lesssim -1.8$ .

The other important parameter we have considered is  $z_{\text{wall}}/H$ , which is related to the height of the disk wall  $Z_{\text{wall}}$  or dust sublimation front, located at the radius where the disk reaches the temperature above which silicates sublimate (§3.2.1.) We have used the excess  $DCE_{J-[4.5]}$  as a probe of the wall height. This is the best band for this purpose, because as can be seen in Figure 12 where the flux at  $4.5 \mu\text{m}$  is indicated, the flux at longer wavelengths ( $5.8 \mu\text{m}$  or  $8.0 \mu\text{m}$ ) includes contributions from the disk, while at  $3.6 \mu\text{m}$  the color excess might be more contaminated by the star.

In Figure 16 the median of  $z_{\text{wall}}/H$  is  $\sim 2, 1.6, 1.3$  and  $1.45$  at 1.5, 2.5, 4.5 and 7.5 Myr, respectively; thus it decreases from bin 1 to bin 3 without a significant change at bin 4. Although the median of  $z_{\text{wall}}/H$  is taken as a representative value of the corresponding distributions, Figure 15 shows that at all age bins there is a wide range of values of  $z_{\text{wall}}/H$ . The peak of the distribution for  $z_{\text{wall}}/H$  in Figure 15 is located at  $z_{\text{wall}}/H \sim 0.6, 0.6, 0.2$  and  $0.2$  for age bins 1, 2, 3 and 4, respectively, and it becomes more pronounced as the age increases. In Ta-

ble 6 we show the mode of the distributions of  $z_{\text{wall}}/H$  shown in Figure 15, and the corresponding range of values of  $Z_{\text{wall}}$  in each age bin, given by  $Z_{\text{wall}_{\text{min}}}$  and  $Z_{\text{wall}_{\text{max}}}$ . As can be seen, even if  $z_{\text{wall}}/H$  stays relatively constant in the older age bins, the physical height of the wall decreases with age (see Table 6). This is because the scale height  $H \propto R_{\text{in}}^{3/2}$ , the sublimation radius  $R_{\text{in}} \propto (L_* + L_{\text{acc}})^{1/2}$ , and the stellar and accretion luminosity decrease with age. The height of the wall is also an indicator of dust settling in the innermost regions of the disk, so our results indicate that the dust in these regions also settle with age.

The criteria we applied in this work to select the observational sample allows us to eliminate PTDs and TDs with large cavities devoid of optically thin dust, i.e., disks with only photospheric near-IR emission. However, we may have included in our analysis a few transitional disks with inner cavities filled with sufficient optical thin material to produce an excess at  $5.8 \mu\text{m}$  and  $8 \mu\text{m}$  that satisfies our observational selection criteria (see §2.3). This is particularly relevant for the older bins, but according to Espaillat et al. (2014), TDs represent  $\sim 10 - 20\%$  of the total population of disks in different stellar groups and this fraction reduces when considering only transitional disks with optical thin material inside their cavities. Moreover disks with inner clearings have relatively high fluxes at  $24 \mu\text{m}$  arising in the frontally illuminated edge of the cavity (Grant et al. 2018); in contrast, our statistical analysis indicates that the flux at  $24 \mu\text{m}$  is sufficiently low to be consistent with a very high degree of settling. A scenario in which the disk flux decreases at all bands due to increased dust settling and growth is more consistent with our evolutionary results.

Although we cannot determine the conditions under which the disks follow the evolved disks scenario vs inner disk clearing, we find that from the initially compiled sample containing diskless as well as disk-bearing stars in all the stellar groups, before applying the selection criteria described in §2.3 to define our disk-bearing stars sample,  $\sim 35\%$  of them were classified as full-disk-bearing stars which have undergone the evolved disk path thus, according to their SEDs, they do not have large inner cavities as transitional disks. The other  $\sim 65\%$  of the stars are either diskless stars, TDs or objects at earlier evolutionary stages such as Class I objects. We examined the sample of stars rejected by our selection criteria from the initial sample, searching for transitional disks - that is, disks without near-IR excess but with  $24 \mu\text{m}$  comparable to that of the Taurus median (Maucó et al. 2016) - and found 4, 4, 5 and 2 TDs, in the age bins 1, 2, 3, and 4, respectively. These transitional disks represent  $\lesssim 1\%$  of the initially compiled sample, in agreement with the low occurrence found in other studies (Espaillat et al. 2014).

#### 4.2. Disk frequency

**Table 6.** Range of values of  $Z_{wall}$ , and mode of the distribution of  $z_{wall}/H$  in each age bin

Age	mode( $z_{wall}/H$ )	$Z_{wall_{min}}$	$Z_{wall_{max}}$	Age
Myr		au	au	bin
1.5	0.6	$3 \times 10^{-3}$	$5.85 \times 10^{-3}$	1
2.5	0.6	$2.02 \times 10^{-3}$	$5.85 \times 10^{-3}$	2
4.5	0.2	$5.1 \times 10^{-4}$	$2 \times 10^{-3}$	3
7.5	0.2	$4.22 \times 10^{-4}$	$2 \times 10^{-3}$	4

Observations of disk frequency (Hernández et al. 2007a; Briceño et al. 2019), indicate that  $\sim 70 - 80\%$  of the stars in young ( $\sim 1$  Myr) stellar groups are disk-bearing stars, while at 5 Myr this fraction drops to  $\sim 15\%$ . For groups older than  $\sim 8$  Myr, only about  $\sim 8\%$  of the disk-bearing stars have survived.

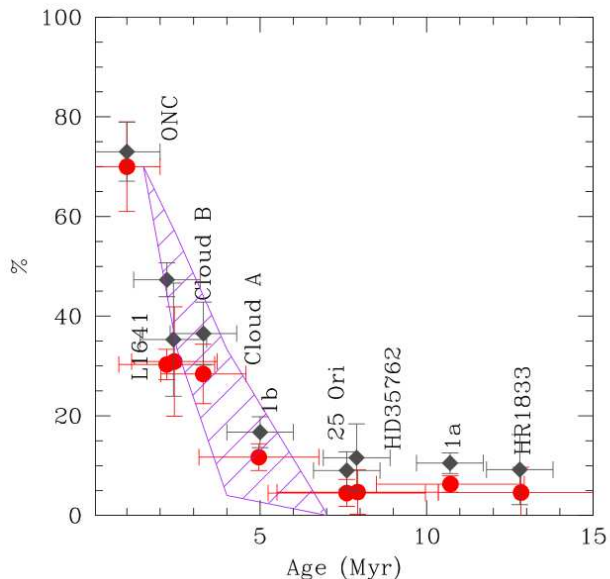


**Figure 18.** Predicted disk frequency as a function of age for disks following viscous evolution and photoevaporation. The purple region shows predictions for  $\dot{M}_{\text{phot,lim}} \sim 3 \times 10^{-9} M_{\odot}/\text{yr}$  (lower boundary) and  $\dot{M}_{\text{phot,lim}} \sim 10^{-9} M_{\odot}/\text{yr}$  (upper boundary). The fraction of accretors (red dots) and the disk fraction (dark gray diamonds) as a function of age for different stellar groups taken from Briceño et al. (2019) are shown for comparison.

In Figure 11 we show that the observed decay of the mass accretion rate is consistent with viscously evolving disks; however, viscous evolution cannot explain the decrease of disk frequency, since it only predicts that the disk will expand while decreasing its surface density with age, and a fraction of the disk material will be accreted onto the star. Another agent driving disk evolution is photoevaporation. The upper levels of the disk are

heated by high energy radiation from the star and accretion shock so that the sound speed becomes higher than the escape velocity. The gas leaves the disk in a photoevaporative wind, at a rate that depends on the radiation field considered to be more effective in driving the wind, either X-rays, FUV or EUV radiation (Alexander et al. 2014, and references therein). Since the mass accretion rate decreases with time as a consequence of disk evolution, it eventually becomes comparable to the mass loss rate in the wind; when this happens, matter from the outer disk flows away instead of reaching the star, while the inner disk quickly drains out onto the star (Clarke et al. 2001). Models of photoevaporative winds predict after this time is reached, the rest of the disk dissipates in time scales smaller than the viscous time scale (Alexander & Armitage 2007; Alexander et al. 2014).

We have attempted to incorporate the effects of photoevaporation in our study of disk evolution in a simple way. Essentially, we allow the disks around the stars in the first age bin to evolve viscously, and assume that they dissipate instantaneously once their mass accretion rate reaches a given limiting value, which would correspond to the photoevaporation mass loss rate. To do this we take the observed distribution of mass accretion rates at bin 1 (upper left panel in Figure 8) and assume a disk fraction of 70% at bin 1 (1.5 Myr) (Briceño et al. 2019). We set a limit for the photoevaporation rate  $\dot{M}_{\text{phot,lim}}$  such that if  $\dot{M} < \dot{M}_{\text{phot,lim}}$ , the disk stops accreting and essentially disappears. We let each bin from the initial distribution of  $\dot{M}$  viscously evolve following equation (5) with  $\alpha=0.01$ ,  $R_1=10$  au and  $M_d(0)=0.07 M_{\odot}$  for a  $0.30 M_{\odot}$  star, which are the values used in constructing the green solid line in Figure 11, but we note that any value of the triad ( $M_d(0)$ ,  $R_1$  and  $\alpha$ ) that fits the observed  $\dot{M}(\text{age})$  with similar  $\chi^2$  (see Fig. 10) leads to the same result, by construction. At each age bin we eliminate the disks with mass accretion rates below  $\dot{M}_{\text{phot,lim}}$  and recalculate the disk fraction. We vary  $\dot{M}_{\text{phot,lim}}$  to achieve a good fit to the observed disk fractions. We find that values of  $\dot{M}_{\text{phot,lim}}$  between  $\sim 10^{-9} M_{\odot}/\text{yr}$  and  $\sim 5 \times 10^{-9} M_{\odot}/\text{yr}$  give a reasonable fit to the observations, as shown in Figure 18, in which we plot the disk fraction and the accretors fraction for different stellar groups as a function of age from Briceño et al. (2019).



A higher value of  $\dot{M}_{\text{phot,lim}}$  would result in a more rapid decay of the disk frequency because disks would disappear much sooner.

As shown in Figure 18 the predicted disk fraction as a function of age follows the observations reasonably well. Our simple treatment predicts no inner disks beyond 7 Myr, possibly because we did not include other mechanisms that may allow the existence of inner disk at these older ages. Disks surviving at ages  $> 7$  Myr may be those that started with higher masses, but detailed calculations including the actual evolution of stars in the presence of photoevaporation are required for a better comparison with observations. A more detailed estimate of the disk frequency will be made in a future work in order to obtain a disk fraction more consistent with the observed values, in particular in the oldest groups. In any case, our results together with Figure 11, suggest that the main agents driving evolution of the gas in the disk are viscous evolution and photoevaporation.

### 4.3. Snowlines

The gas component of the disk contains atoms and molecules of different species, some of which sublimate at relatively low temperatures ( $\lesssim 150$  K); these species are known as *volatiles*. These volatiles seem to play a major role in the process of planet formation, giving rise to an active chemistry that influences the composition of the planets' atmospheres during their formation process. The disk radius where a certain volatile reaches its sublimation temperature is called snowline or condensation front. Outside the snowline the volatiles are frozen, adhered to the surface of dust grains, and inside the snowline they remain in the gas phase. In the last decade, studying the location of different snowlines has gained attention, in particular to explain the chemical composition of some exoplanetary atmospheres, since it depends directly on the available molecules in the surrounding regions of the planets, during their formation process (Öberg et al. 2011; Ali-Dib et al. 2014; Madhusudhan et al. 2014). It has also been suggested that an enhancement of dust growth can occur near the location of different condensation fronts, favoring the accumulation of mm to dm grains, which might eventually form planetesimals (Zhang et al. 2015; Okuzumi et al. 2016).

Some authors have found that the shape and location of the different snowlines are influenced by changes in the gas surface density (Piso et al. 2015; Krijt et al. 2016; Powell et al. 2017). Molecules such as CO and its isotopologues have been observed and measured (Qi et al. 2011, 2013, 2015), and while the H<sub>2</sub>O snowline is far more difficult to detect and study because it is located very close to the star, they are both important to understand their influence in the dust component of the disk, the chemical abundances in exoplanetary atmospheres, and also the composition of the planets and asteroids in the Solar System. A more general overview

about the different theoretical and observational aspects of snowlines can be found in Pontoppidan et al. (2014).

We study the location and evolution of different snowlines, in particular H<sub>2</sub>O and CO, under the assumption that the gas and the dust in the disk follow the same temperature distribution.

For each model in our grid we calculate self consistently the vertical and radial structure of the disk (see §3.1.2), which allows us to find the shape and location of the different snowlines. We take the density-dependent sublimation temperature for water ice reported in Table 3 from Pollack et al. (1994) and for CO we adopt 20 K following Öberg et al. (2011) and Qi et al. (2011, 2013, 2015). Figure 19 shows the shape and location of the H<sub>2</sub>O and CO snowlines, for disk models, which we refer to as mean models, calculated using the median observed values of the mass accretion rate (from Table 4 and Figure 9) and the median  $\epsilon$  parameter found in this work (right panel in Figure 16) at the different age bins. The snowlines are not vertical sublimation fronts, but they curve towards large radii as the height above the midplane increases, which is a consequence of the vertical temperature gradient in irradiated disks in which the temperature increases towards the disk surface (D'Alessio et al. 1998, 2006). As disks become older, the midplane snowline moves inwards because the stellar and the accretion luminosity decrease (Fig. 4) and the inner disk becomes colder, allowing certain volatiles to remain frozen closer to the star. There is an additional effect in the H<sub>2</sub>O snowline which is more accentuated in the disk models with the highest mass accretion rates (e.g. at bin 1), in which the snowline moves inwards as  $z/R$  decreases from the disk surface to the midplane, but at  $0 \lesssim z/R \lesssim 0.03$  is pushed outwards, from  $\sim 0.4$  au at  $z/R \sim 0.03$  to  $\sim 0.7$  au at the very midplane ( $z/R = 0$ ). At bin 4 the midplane snowline is pushed from  $\sim 0.17$  au at  $z/R \sim 0.02$  up to 0.29 au at  $z/R = 0$ . This effect is stronger in the first two age bins and it is a consequence of viscous dissipation, since the higher the mass accretion rate, the more efficient the viscous heating in this region (D'Alessio et al. 1998, 2001, 2006; Drkażkowska & Alibert 2017; Huang et al. 2017; Pinte et al. 2018). Figure 19 also shows the location of 1 and of 3 scale heights  $H$  (white dashed lines), evaluated at the midplane temperature; it can be seen that the scale height decreases with age. Figure 20 shows the location of the H<sub>2</sub>O and CO snowlines; this value depends on  $z/R$  as already noticed, thus we show the location for different values of  $z/R$ : 0 (blue), 0.25 (black), and 0.4 (magenta). The snowline location decreases with age, except for the case  $z/R = 0.25$  for the CO snowline, where it remains approximately constant.

Table 7 shows the midplane snowline location for H<sub>2</sub>O and CO at the different age bins. At 1.5, 2.5, 4.5, and 7.5 Myr the water snowline is located at  $\sim 0.7, 0.6, 0.31,$  and 0.29 au, respectively, while the CO snowline is located at  $\sim 15, 7, 5,$  and 3.5 au. Qi et al. (2013) reported

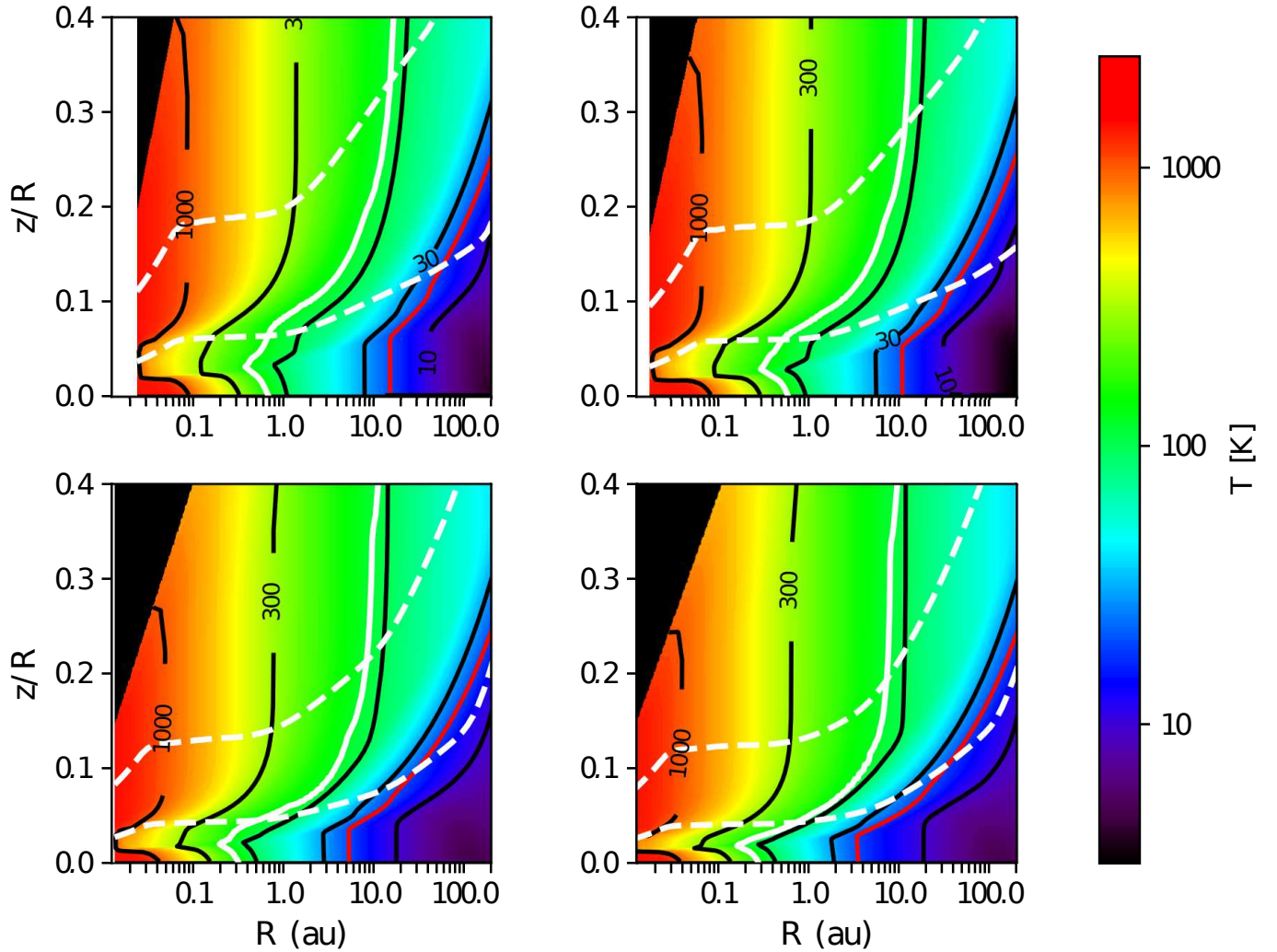


**Figure 19.** Location and shape of the H<sub>2</sub>O (white solid line) and CO (red solid line) snowlines for disk models calculated for the median mass accretion rate  $\dot{M}$  and median settling parameter  $\epsilon$  at each age bin, with bin 1 (upper left), bin 2 (upper right), bin 3 (lower left) and bin 4 (lower right). The color scale shows the temperature distribution with temperature iso-contours for 10, 30, 100, 300, 1000 K (black lines). The white dashed lines show the location of 1 and of 3 scale heights at each radius.

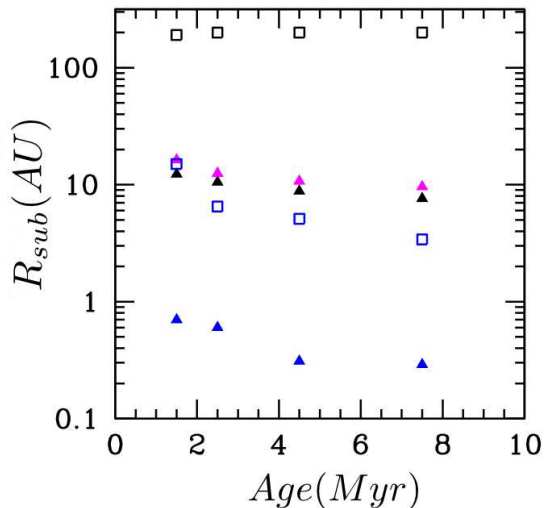


**Figure 20.** Location of the H<sub>2</sub>O (solid triangles) and CO (empty squares) snowlines, for different values of  $z/R$ : 0 (blue), 0.25 (black) and 0.4 (magenta).

**Table 7.** Midplane location of the H<sub>2</sub>O and CO snowlines

Age	$R_{\text{sub,H}_2\text{O}}$	$R_{\text{sub,CO}}$
Myr	au	au
1.5	0.7	15
2.5	0.6	7
4.5	0.31	5
7.5	0.29	3.5

a  $R_{\text{sub,CO}} \sim 30$  au for the  $\sim 10$  Myr old disk around TW Hya, whereas Schwarz et al. (2016) located the CO midplane snowline at  $\sim 17 - 23$  au, using ALMA observations of CO isotopologues, for the same source. Notice that the disk around TW Hya is a transitional disk, with an inner hole of  $\sim 4$  au (see Espaillat et al. 2014), which should be hotter than the disks from our mean models, since TW Hya has a  $0.8 M_{\odot}$  star which irradiates directly the disk wall, while our calculations were made for a  $0.3 M_{\odot}$  star surrounded by a full disk; and this might explain the difference in the locations we find for the CO snowline. The location of the snowlines, determined with observations, is sensitive to the disk depth at which the emission of the volatiles is being detected; our models show that at  $z/R \sim 0.06$  au,  $R_{\text{sub,CO}} \sim 13$  au while at  $z/R \sim 0.12$  au,  $R_{\text{sub,CO}} \sim 40$  au at bin 4 (7.5 Myr). Mulders et al. (2015) calculate the H<sub>2</sub>O snowline for disks with different dust grain sizes, and find an analytical expression for two regimes of the maximum grain

sizes: ISM-like and cm-sized grains. The values they find range from 0.28-0.60 au (1.5 Myr), 0.22-0.49 au (2.5 Myr), 0.11-0.23 au (4.5 Myr) and 0.07-0.16 au (7.5 Myr) for a  $0.30 M_{\odot}$  star, which are similar to our results (Table 7). The location of the snowlines at the different age bins may put constraints on the timescale for the formation of planets within the inner au in the disk.

## 5. SUMMARY AND CONCLUSIONS

- We performed a statistical study focused on the global evolution of protoplanetary disks around T Tauri stars, that includes observed mass accretion rates as a constraint to infer the inner disk properties. The observational sample includes various stellar groups with IRAC and MIPS 24 photometry, as well as PANSTARRS  $[g - i]$  color (used to calculate  $A_V$  uniformly for most stars), with ages from 1 to 11 Myr, and located at distances  $\lesssim 500$  pc.
- By introducing the disk color excess (DCE) as an indicator of infrared excess, we study the evolution of the observed IR emission from the disk-bearing stars in the stellar groups, separated into different age bins (1.5, 2.5, 4.5 and 7.5 Myr) to make a more robust statistical study at each age. The median of the different DCEs decreases as the age of the bin increases.
- We use a different sample of TTSSs with significant overlap with the DCEs sample, and with additional GAIA DR2 distances, to determine mass accretion rates using the EW of the H $\alpha$  line, which was either available from previous works, or determined by us. The observed decay of  $\dot{M}$  with age is consistent with viscously evolving disks; in particular we find a good fit to the observed disks data for a viscosity coefficient  $\alpha = 0.01$ , an initial disk mass  $M_d(0) = 0.07 M_{\odot}$ , and a characteristic radius  $R_1 = 10$  au, inside which 60% of the initial disk mass is located. Additionally, different combinations of the triad  $(M_d(0), R_1, \alpha)$  can also provide a good match as determined from the  $\chi^2$  value in Figure 10.
- Using the D'Alessio irradiated accretion disk (DIAD) models, we computed, for each age bin, a grid of disk models varying the degree of dust settling  $\epsilon$ , the mass accretion rate  $\dot{M}$ , the parameter  $z_{\text{wall}}/H$  related to the height of the wall, and the cosine of the inclination angle  $\cos(i)$ . We incorporated a two-layered wall to emulate the wall curvature, as well as an exponential tapering at the outer edge of the disk. Using this grid we computed synthetic DCEs in order to forward model the observed DCEs distributions. The observed  $\dot{M}$  distributions at the different age bins are implemented as constraints in the method.

- The distributions of the parameters  $\epsilon$ , which measures the dust depletion in the upper disk layers, and  $z_{wall}/H$ , which measures the height of the wall at the dust destruction radius, show that even at 1.5 Myr (bin 1) a fraction of the disks are highly settled ( $\log(\epsilon) \lesssim -3.0$ ) with low walls ( $z_{wall}/H \lesssim 1$ ), and the fraction of these disks increases with age; also the peak of the distributions moves towards smaller values.
- We make a first attempt to test photoevaporation by letting the observed distribution of  $\dot{M}$  from bin 1 viscously evolve, and we set a photoevaporation mass loss rate  $\dot{M}_{\text{phot,lim}}$  below which the star stops accreting material from the disk. We find that  $\dot{M}_{\text{phot,lim}} \sim 1 - 3 \times 10^{-9} M_{\odot} \text{yr}^{-1}$  fits reasonably well the observed decay of the disk and accretors fractions with age.
- We find that the H<sub>2</sub>O and CO snowlines curve towards larger radii as the height over the disk midplane increases because of the vertical temperature gradient. At  $0 \lesssim z/R \lesssim 0.02$ , the H<sub>2</sub>O snowline is pushed outwards due to viscous dissipation. The snowlines migrate inwards as the disk evolves, as

a consequence of the decrease in the stellar and accretion shocks luminosity with age. The H<sub>2</sub>O midplane snowline starts at  $\sim 0.7$  au at 1.5 Myr and ends up at  $\sim 0.29$  au at 7.5 Myr; the CO midplane snowline starts at  $\sim 15$  au at 1.5 Myr and ends up at  $\sim 3.5$  au at 7.5 Myr for the the models with the median mass accretion rate  $\dot{M}$  and median degree of settling  $\log(\epsilon)$  at each age bin.

We thank an anonymous referee for comments and suggestions that greatly improved the presentation of this paper. We also thank Tom Megeath for providing infrared photometry for the ONC, Kevin Luhman for providing intrinsic photospheric colors for early K-type stars, and Lee Hartmann and Jaehan Bae for insightful conversations. E.M.M. and S.L. acknowledge support from PAPIIT-UNAM IN101418 and CONACyT 23861. E.M. M. acknowledges support from a CONACyT scholarship. J.H acknowledges support from PAPIIT-UNAM IA102319. N. C. acknowledges partial support from NASA grant NNX17AE57G. K.M. acknowledges financial support from FONDECYT-CONICYT project no. 3190859 and from the ICM (Iniciativa Científica Milenio) via the Núcleo Milenio de Formación Planetaria grant.



Table 8. Stellar properties

2MASS	SpT	$A_V$	$T_{\text{eff}}(\text{K})$	Ref	$L_*/L_\odot$	$M_*/M_\odot$	$R_*/R_\odot$	dist(pc)	EW H $\alpha$ (Å)	$DCE_{J-[4.5]}$	$DCE_{J-[5.8]}$	$DCE_{J-[8.0]}$	$DCE_{J-[24]}$	$\dot{M}(M_\odot \text{ yr}^{-1})$
ONC														
05341189-0506162	M5.5	0.55	2740	1	0.03	...	...	416	-105.8	$0.49 \pm 0.04$	$0.88 \pm 0.05$	$1.69 \pm 0.05$	$4.2 \pm 0.09$	...
05342125-0450326	M3.5	1.4	3260	1	0.03	0.18	0.58	245	-15.0	$0.21 \pm 0.03$	$0.55 \pm 0.04$	$1.61 \pm 0.04$	$6.16 \pm 0.04$	$1.06 \times 10^{-10}$
05372601-0534013	K3.5	0.6	4440	2	0.81	1.14	1.52	382	-3.0	...	...	...	...	$2.91 \times 10^{-10}$
05334954-0536208	K5.5	1.0	4080	1	0.43	0.81	1.31	404	-5.8	$1.73 \pm 0.02$	$2.19 \pm 0.02$	$2.87 \pm 0.02$	$4.77 \pm 0.03$	$3.30 \times 10^{-10}$
05352720-0530247	M5.0	1.69	2880	4	0.44	...	...	415	...	$0.23 \pm 0.05$	$0.58 \pm 0.05$	$1.43 \pm 0.05$	...	...
Taurus														
04270469+2606163	K6.0	0.0	4020	5	...	0.72	1.92	121	-42.8	...	...	...	...	$8.02 \times 10^{-9}$
04141700+2810578	K3.0	2.36	4550	5	1.03	1.21	1.63	132	-90.7	$2.98 \pm 0.07$	$3.32 \pm 0.07$	$3.88 \pm 0.07$	$6.61 \pm 0.08$	$1.15 \times 10^{-8}$
04231822+2641156	M3.5	4.4	3260	5	...	...	...	...	...	$1.24 \pm 0.1$	$1.55 \pm 0.1$	$2.22 \pm 0.1$	$5.5 \pm 0.11$	...

NOTE—This table is published in its entirety in the electronic edition of the *Astrophysical Journal*. A portion is shown here for guidance regarding its form and content.

NOTE—The errors associated to the DCEs are based only on the photometric errors and thus they are underestimated.

NOTE—References for spectral types (column 5): 1. Hernández et al. 2020a (in preparation), 2. Briceño et al. (2019), 3. Hillenbrand (1997), 4. Hillenbrand et al. (2013), 5. Esplin et al. (2014), 6. Lada et al. (2006), 7. Hernández et al. (2014), 8. Bayo et al. (2008), 9. Bayo et al. (2011), 10. Luhman & Mamajek (2012), 11. Spina et al. (2014), 12. This work.

NOTE—The data for the EW H $\alpha$  comes from: Hernández et al. 2020a (in preparation) (ONC), this work (Taurus), Hernández et al. (2014) ( $\sigma$  Ori) and Briceño et al. (2019) (Ori OB1b and Ori OB1a).

## REFERENCES

- Alcalá, J. M., Natta, A., Manara, C. F., et al. 2014, *A&A*, 561, A2
- Alexander, R., Pascucci, I., Andrews, S., Armitage, P., & Cieza, L. 2014, in *Protostars and Planets VI*, ed. H. Beuther, R. S. Klessen, C. P. Dullemond, & T. Henning, 475
- Alexander, R. D., & Armitage, P. J. 2007, *MNRAS*, 375, 500
- Ali-Dib, M., Mousis, O., Petit, J.-M., & Lunine, J. I. 2014, *ApJ*, 785, 125
- ALMA Partnership, Brogan, C. L., Pérez, L. M., et al. 2015, *ApJL*, 808, L3
- Andrews, S. M., & Williams, J. P. 2005, *ApJ*, 631, 1134
- Andrews, S. M., Wilner, D. J., Zhu, Z., et al. 2016, *ApJL*, 820, L40
- Andrews, S. M., Huang, J., Pérez, L. M., et al. 2018, *ApJL*, 869, L41
- Bailer-Jones, C. A. L. 2015, *PASP*, 127, 994
- Bayo, A., Rodrigo, C., Barrado Y Navascués, D., et al. 2008, *A&A*, 492, 277
- Bayo, A., Barrado, D., Stauffer, J., et al. 2011, *A&A*, 536, A63
- Birnstiel, T., Dullemond, C. P., & Brauer, F. 2009, *A&A*, 503, L5
- . 2010, *A&A*, 513, A79
- Birnstiel, T., Klahr, H., & Ercolano, B. 2012, *A&A*, 539, A148
- Birnstiel, T., Ormel, C. W., & Dullemond, C. P. 2011, *A&A*, 525, A11
- Briceño, C., Calvet, N., Hernández, J., et al. 2019, *AJ*, 157, 85
- Calvet, N., D’Alessio, P., Hartmann, L., et al. 2002, *ApJ*, 568, 1008
- Calvet, N., & Gullbring, E. 1998, *ApJ*, 509, 802
- Calvet, N., Patino, A., Magris, G. C., & D’Alessio, P. 1991, *ApJ*, 380, 617
- Calvet, N., D’Alessio, P., Watson, D. M., et al. 2005, *ApJL*, 630, L185
- Cardelli, J. A., Clayton, G. C., & Mathis, J. S. 1989, *ApJ*, 345, 245
- Chambers, K. C., Magnier, E. A., Metcalfe, N., et al. 2016, *arXiv e-prints*, arXiv:1612.05560
- Chiang, E., & Murray-Clay, R. 2007, *Nature Physics*, 3, 604
- Cieza, L., Padgett, D. L., Stapelfeldt, K. R., et al. 2007, *ApJ*, 667, 308
- Clarke, C. J., Gendrin, A., & Sotomayor, M. 2001, *MNRAS*, 328, 485
- Currie, T., Lada, C. J., Plavchan, P., et al. 2009, *ApJ*, 698, 1
- Cutri, R. M., Skrutskie, M. F., van Dyk, S., et al. 2003, *VizieR Online Data Catalog*, II/246
- Da Rio, N., Robberto, M., Soderblom, D. R., et al. 2010, *ApJ*, 722, 1092
- D’Alessio, P., Calvet, N., & Hartmann, L. 2001, *ApJ*, 553, 321
- D’Alessio, P., Calvet, N., Hartmann, L., Franco-Hernández, R., & Servín, H. 2006, *ApJ*, 638, 314
- D’Alessio, P., Calvet, N., Hartmann, L., Lizano, S., & Cantó, J. 1999, *ApJ*, 527, 893
- D’Alessio, P., Cantó, J., Calvet, N., & Lizano, S. 1998, *ApJ*, 500, 411
- D’Alessio, P., Hartmann, L., Calvet, N., et al. 2005, *ApJ*, 621, 461
- David, T. J., Hillenbrand, L. A., Gillen, E., et al. 2019, *ApJ*, 872, 161
- Draine, B. T., & Lee, H. M. 1984, *ApJ*, 285, 89
- Drkażkowska, J., & Alibert, Y. 2017, *A&A*, 608, A92
- Dullemond, C. P., & Dominik, C. 2004, *A&A*, 421, 1075
- . 2005, *A&A*, 434, 971
- Dullemond, C. P., & Monnier, J. D. 2010, *ARA&A*, 48, 205
- Ercolano, B., Koepferl, C., Owen, J., & Robitaille, T. 2015, *MNRAS*, 452, 3689
- Espaillet, C., Calvet, N., D’Alessio, P., et al. 2007, *ApJL*, 670, L135
- Espaillet, C., D’Alessio, P., Hernández, J., et al. 2010, *ApJ*, 717, 441
- Espaillet, C., Ingleby, L., Hernández, J., et al. 2012, *ApJ*, 747, 103
- Espaillet, C., Muzerolle, J., Najita, J., et al. 2014, in *Protostars and Planets VI*, ed. H. Beuther, R. S. Klessen, C. P. Dullemond, & T. Henning, 497
- Esplin, T. L., Luhman, K. L., & Mamajek, E. E. 2014, *ApJ*, 784, 126
- Fairlamb, J. R., Oudmaijer, R. D., Mendigutia, I., Ilee, J. D., & van den Ancker, M. E. 2017, *MNRAS*, 464, 4721
- Fazio, G. G., Hora, J. L., Allen, L. E., et al. 2004, *ApJS*, 154, 10
- Fedele, D., van den Ancker, M. E., Henning, T., Jayawardhana, R., & Oliveira, J. M. 2010, *A&A*, 510, A72
- Franciosini, E., Sacco, G. G., Jeffries, R. D., et al. 2018, *A&A*, 616, L12
- Frasca, A., Biazzo, K., Lanzafame, A. C., et al. 2015, *A&A*, 575, A4
- Furlan, E., Hartmann, L., Calvet, N., et al. 2006, *ApJS*, 165, 568
- Furlan, E., Watson, D. M., McClure, M. K., et al. 2009, *ApJ*, 703, 1964

- Furlan, E., Luhman, K. L., Espaillat, C., et al. 2011, *ApJS*, 195, 3
- Gaia Collaboration, Brown, A. G. A., Vallenari, A., et al. 2018, *A&A*, 616, A1
- Galli, P. A. B., Joncour, I., & Moraux, E. 2018, *MNRAS*, 477, L50
- Galli, P. A. B., Loinard, L., Bouy, H., et al. 2019, *A&A*, 630, A137
- Grant, S. L., Espaillat, C. C., Megeath, S. T., et al. 2018, *ApJ*, 863, 13
- Haffert, S. Y., Bohn, A. J., de Boer, J., et al. 2019, *Nature Astronomy*, 3, 749
- Hartmann, L., Calvet, N., Gullbring, E., & D'Alessio, P. 1998, *ApJ*, 495, 385
- Hartmann, L., Herczeg, G., & Calvet, N. 2016, *ARA&A*, 54, 135
- Hartmann, L., Megeath, S. T., Allen, L., et al. 2005, *ApJ*, 629, 881
- Herbst, W. 2008, *Star Formation in IC 348*, ed. B. Reipurth, Vol. 4, 372
- Hernandez, J., Briceño, C., Calvet, N., et al. 2017, *SPTCLASS: SPecTral CLASSificator code*, , , ascl:1705.005
- Hernández, J., Calvet, N., Briceño, C., Hartmann, L., & Berlind, P. 2004, *AJ*, 127, 1682
- Hernández, J., Hartmann, L., Calvet, N., et al. 2008, *ApJ*, 686, 1195
- Hernández, J., Morales-Calderon, M., Calvet, N., et al. 2010, *ApJ*, 722, 1226
- Hernández, J., Hartmann, L., Megeath, T., et al. 2007a, *ApJ*, 662, 1067
- Hernández, J., Calvet, N., Briceño, C., et al. 2007b, *ApJ*, 671, 1784
- Hernández, J., Calvet, N., Perez, A., et al. 2014, *ApJ*, 794, 36
- Hillenbrand, L. A. 1997, *AJ*, 113, 1733
- Hillenbrand, L. A., Hoffer, A. S., & Herczeg, G. J. 2013, *AJ*, 146, 85
- Huang, J., Öberg, K. I., Qi, C., et al. 2017, *ApJ*, 835, 231
- Ingleby, L., Calvet, N., Bergin, E., et al. 2011, *ApJ*, 743, 105
- Ingleby, L., Calvet, N., Herczeg, G., et al. 2013, *ApJ*, 767, 112
- Isella, A., & Natta, A. 2005, *A&A*, 438, 899
- Jeffries, R. D., Jackson, R. J., Franciosini, E., et al. 2017, *MNRAS*, 464, 1456
- Keppler, M., Teague, R., Bae, J., et al. 2019, *A&A*, 625, A118
- Koepferl, C. M., Ercolano, B., Dale, J., et al. 2013, *MNRAS*, 428, 3327
- Kounkel, M., Covey, K., Suárez, G., et al. 2018, *AJ*, 156, 84
- Krijt, S., Ciesla, F. J., & Bergin, E. A. 2016, *ApJ*, 833, 285
- Lada, C. J., Muench, A. A., Luhman, K. L., et al. 2006, *AJ*, 131, 1574
- Long, F., Pinilla, P., Herczeg, G. J., et al. 2018, *ApJ*, 869, 17
- Long, F., Herczeg, G. J., Harsono, D., et al. 2019, *ApJ*, 882, 49
- Luhman, K. L. 2004, *ApJ*, 602, 816
- Luhman, K. L., Allen, P. R., Espaillat, C., Hartmann, L., & Calvet, N. 2010, *ApJS*, 186, 111
- Luhman, K. L., & Mamajek, E. E. 2012, *ApJ*, 758, 31
- Luhman, K. L., & Rieke, G. H. 1999, *ApJ*, 525, 440
- Lynden-Bell, D., & Pringle, J. E. 1974, *MNRAS*, 168, 603
- Madhusudhan, N., Amin, M. A., & Kennedy, G. M. 2014, *ApJL*, 794, L12
- Manoj, P., Kim, K. H., Furlan, E., et al. 2011, *ApJS*, 193, 11
- Marjoram, P., Hamblin, S., & Foley, B. 2015, 47, 176
- Maucó, K., Hernández, J., Calvet, N., et al. 2016, *ApJ*, 829, 38
- McClure, M. K., Furlan, E., Manoj, P., et al. 2010, *ApJS*, 188, 75
- McClure, M. K., D'Alessio, P., Calvet, N., et al. 2013, *ApJ*, 775, 114
- Megeath, S. T., Gutermuth, R., Muzerolle, J., et al. 2012, *AJ*, 144, 192
- . 2016, *AJ*, 151, 5
- Merín, B., Brown, J. M., Oliveira, I., et al. 2010, *ApJ*, 718, 1200
- Mulders, G. D., Ciesla, F. J., Min, M., & Pascucci, I. 2015, *ApJ*, 807, 9
- Muzerolle, J., Allen, L. E., Megeath, S. T., Hernández, J., & Gutermuth, R. A. 2010, *ApJ*, 708, 1107
- Öberg, K. I., Murray-Clay, R., & Bergin, E. A. 2011, *ApJL*, 743, L16
- Okuzumi, S., Momose, M., Sirono, S.-i., Kobayashi, H., & Tanaka, H. 2016, *ApJ*, 821, 82
- Ortiz-León, G. N., Loinard, L., Dzib, S. A., et al. 2018, *ApJ*, 865, 73
- Owen, J. E. 2016, *PASA*, 33, e005
- Pecaut, M. J., & Mamajek, E. E. 2013, *ApJS*, 208, 9
- Pecaut, M. J., Mamajek, E. E., & Bubar, E. J. 2012, *ApJ*, 746, 154
- Pérez-Blanco, A., Maucó, K., Hernández, J., et al. 2018, *ApJ*, 867, 116
- Pinilla, P., Flock, M., Ovelar, M. d. J., & Birnstiel, T. 2016, *A&A*, 596, A81
- Pinte, C., Ménard, F., Duchêne, G., et al. 2018, *A&A*, 609, A47

- Piso, A.-M. A., Öberg, K. I., Birnstiel, T., & Murray-Clay, R. A. 2015, *ApJ*, 815, 109
- Pollack, J. B., Hollenbach, D., Beckwith, S., et al. 1994, *ApJ*, 421, 615
- Pontoppidan, K. M., Salyk, C., Bergin, E. A., et al. 2014, in *Protostars and Planets VI*, ed. H. Beuther, R. S. Klessen, C. P. Dullemond, & T. Henning, 363
- Powell, D., Murray-Clay, R., & Schlichting, H. E. 2017, *ApJ*, 840, 93
- Preibisch, T., Brown, A. G. A., Bridges, T., Guenther, E., & Zinnecker, H. 2002, *AJ*, 124, 404
- Preibisch, T., & Mamajek, E. 2008, *The Nearest OB Association: Scorpius-Centaurus (Sco OB2)*, ed. B. Reipurth, Vol. 5, 235
- Prisinzano, L., Damiani, F., Micela, G., et al. 2016, *A&A*, 589, A70
- Qi, C., D'Alessio, P., Öberg, K. I., et al. 2011, *ApJ*, 740, 84
- Qi, C., Öberg, K. I., Andrews, S. M., et al. 2015, *ApJ*, 813, 128
- Qi, C., Öberg, K. I., Wilner, D. J., et al. 2013, *Science*, 341, 630
- Reipurth, B. 2008, *Handbook of Star Forming Regions, Volume II: The Southern Sky*, Vol. 5
- Rieke, G. H., Young, E. T., Engelbracht, C. W., et al. 2004, *ApJS*, 154, 25
- Sacco, G. G., Franciosini, E., Randich, S., & Pallavicini, R. 2008, *A&A*, 488, 167
- Schwarz, K. R., Bergin, E. A., Cleaves, L. I., et al. 2016, *ApJ*, 823, 91
- Shakura, N. I., & Sunyaev, R. A. 1973, *A&A*, 500, 33
- Siess, L., Dufour, E., & Forestini, M. 2000, *A&A*, 358, 593
- Smiljanic, R., Romano, D., Bragaglia, A., et al. 2016, *A&A*, 589, A115
- Song, I., Zuckerman, B., & Bessell, M. S. 2012, *AJ*, 144, 8
- Spina, L., Randich, S., Palla, F., et al. 2014, *A&A*, 567, A55
- Strom, K. M., Newton, G., Strom, S. E., et al. 1989, *ApJS*, 71, 183
- Tannirkulam, A., Monnier, J. D., Millan-Gabet, R., et al. 2008, *ApJL*, 677, L51
- Testi, L., Birnstiel, T., Ricci, L., et al. 2014, in *Protostars and Planets VI*, ed. H. Beuther, R. S. Klessen, C. P. Dullemond, & T. Henning, 339
- Tobin, J. J., Sheehan, P. D., Megeath, S. T., et al. 2020, *ApJ*, 890, 130
- Tonry, J. L., Stubbs, C. W., Lykke, K. R., et al. 2012, *ApJ*, 750, 99
- Turner, B., & Van Zandt, T. 2012, *Journal of Mathematical Psychology*, 56, 69
- Weidenschilling, S. J. 1997, *Icarus*, 127, 290
- Williams, J. P., & Cieza, L. A. 2011, *ARA&A*, 49, 67
- Zhang, K., Blake, G. A., & Bergin, E. A. 2015, *ApJL*, 806, L7
- Zhang, S., Zhu, Z., Huang, J., et al. 2018, *ApJL*, 869, L47
- Zhu, Z., Nelson, R. P., Dong, R., Espaillat, C., & Hartmann, L. 2012, *ApJ*, 755, 6
- Zhu, Z., Nelson, R. P., Hartmann, L., Espaillat, C., & Calvet, N. 2011, *ApJ*, 729, 47